Article

Synthesis, Characterization, and Biological Profiling of Ruthenium(II)-Based 4-Nitro- and 4-Amino-1,8-naphthalimide Conjugates

Robert B. P. Elmes,* Gary J. Ryan, Maria Luisa Erby, Daniel O. Frimannsson, Jonathan A. Kitchen, Mark Lawler, D. Clive Williams, Susan J. Quinn,* and Thorfinnur Gunnlaugsson*

Read Online

ACCESS | Metrics & More | Article Recommendations | Supporting Information

ABSTRACT: We report the synthesis, photophysical characterization, and biological evaluation of four DNA-binding ruthenium-(II) polypyridyl 4-nitro- and 4-amino-1,8-naphthalimide conjugates. A meta arrangement around the ring connecting the 1,8-naphthalimide to a bipyridine ligand creates a cleft, the result of which renders the shape of the complex complementary to that of DNA. We have demonstrated that each complex exhibits water solubility and a distinctive set of photophysical properties that has allowed the nature of their interaction with DNA to be probed by various ground- and excited-state titrations. Furthermore, by varying the ancillary ligands, we also demonstrate their ability to act as DNA photocleavers, where all compounds have been found to cleave supercoiled DNA with high efficiency. Detailed cellular uptake experiments revealed that the conjugates accumulate in the cytoplasm and nucleus of HeLa cells, showing characteristic red metal-to-ligand charge-transfer emission, and also exhibit photoactivated cytotoxicity within the cells upon irradiation at 450 nm. A comparison between the meta and para arrangements of the 1,8-naphthalimide moiety relative to the Ru(II) center suggests increased DNA binding in the case of the meta arrangement; however, bipyridine−4-amino-1,8-naphthalimide conjugates appear to show superior phototoxicity in comparison to their 4-nitro derivatives.

DNA photocleavage

vs.

DNA binding

Cellular phototoxicity
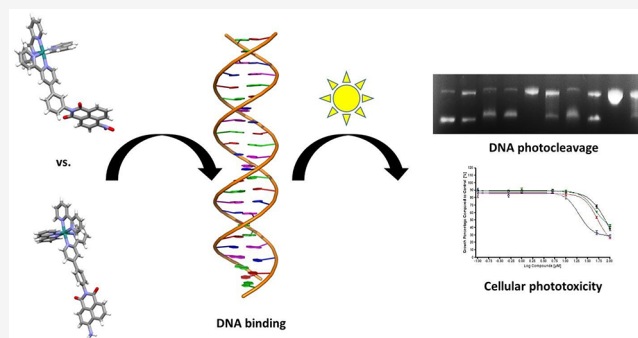
INTRODUCTION

Ruthenium(II) polypyridyl complexes have been extensively studied in recent years for the most part because of their rich photophysical characteristics, which enable their application in diverse scientific disciplines such as solar energy conversion,[1,2] photocatalysis,[3,4] molecular machines,[5,6] and biological imaging,[7−9] to name just a few key areas. With their cationic nature and well-defined spatial geometry, ruthenium(II) polypyridyls are well-known to bind to nucleic acids and, through modulation of their photophysical properties, are capable of reporting on the binding event.[10−15] Several research groups have contributed to a detailed understanding of the binding of such complexes to oligonucleotides through combinations of various spectroscopic methods and biochemical investigations.[16−22] This work has also provided detailed mechanistic insight into their photochemistry with oligonucleotides that often result in photocleavage of DNA through oxidation and/or photoadduct formation.[23−25] Indeed, the inherent excited-state reactivity of π-deficient ruthenium(II) polypyridyls has led to increasing interest in ruthenium(II) polypyridyl complexes as potential photodynamic therapy (PDT) agents.[26−30] Such ruthenium(II) complexes display many properties that make them a promising class of PDT agents,

showing water solubility, photostability, reduced dark toxicity, useful spectroscopic properties, and significant DNA binding affinity.[31−36] However, unlike classical PDT agents, ruthenium-(II) polypyridyl complexes can also initiate apoptosis in cells by other means than through singlet oxygen activation, as recently outlined by us and others in the field.[37−42] In fact, often more than one activation pathway is available to such potential therapeutics, which makes ruthenium(II) polypyridyl complexes highly versatile and exciting therapeutic agents for cancer and other diseases. The study of such agents in vitro and in vivo has been extensively featured in the review by Poynton and co-workers among others.[7,43−46]

Our interest in ruthenium(II) polypyridyls has focused on novel ruthenium(II) conjugates, where tethering the metal center to various other functional subunits such as gold
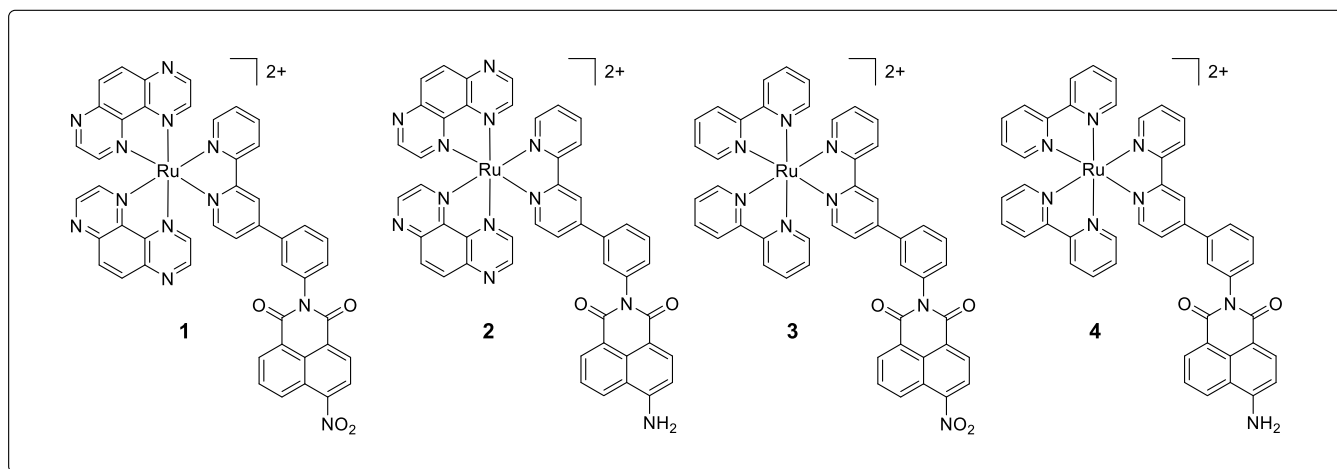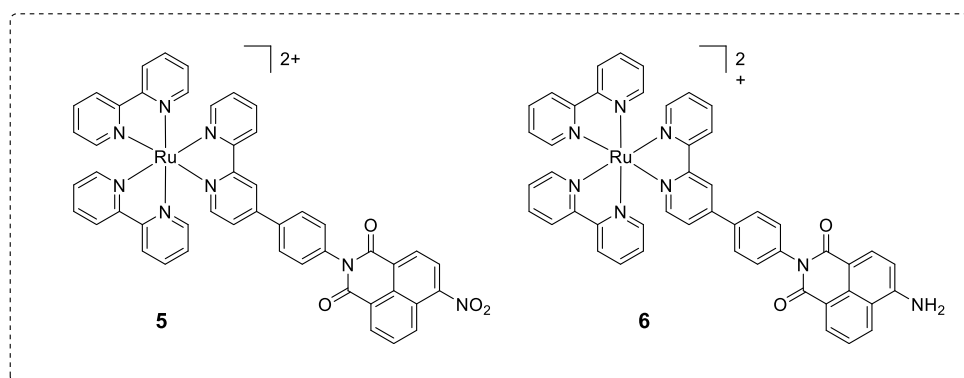
Figure 1. Novel ruthenium(II) 1,8-naphthalimide conjugates **1−4** and previously reported complexes **5** and **6**.[53]

nanoparticles,[47,48] Tröger's bases,[49,50] and appended organic chromophores[51−53] has yielded various modified designs that display high-affinity DNA targeting, enhanced photophysical properties, and effective DNA photocleavage that we have shown can affect numerous biological pathways and initiate apoptosis. We have also investigated the various binding modes of metal-ion complexes with oligonucleotides using ultrafast spectroscopy such as transient IR and transient absorption.[19,23] Recent reports point to the importance of the binding mode of the metal center to DNA to enable the most efficient photoreaction and thus DNA cleavage.[19,37] Indeed, the number of attached chromophores and the nature of the linker between the metal center and appended organic groups appear to strongly affect the subsequent photoreactivity.[52] An example of this was previously reported in the case of rigid linear ruthenium polypyridyl complexes with a 4-nitro- or 4-amino-1,8-naphthalimide appended group; see Figure 1 (**5** and **6**).[53] These complexes were found to cleave plasmid DNA upon visible-light excitation, where the substituent was found to determine the extent of DNA cleavage with the nitro derivative, resulting in the nicking of DNA, while the amino derivative resulted in the formation of nicked and linear DNA.

The 4-nitro- or 4-amino-1,8-naphthalimide compounds are in their own right important therapeutics, as we and others have shown in the past, being able to induce apoptosis and other biological processes.[54−58] The internal charge-transfer excited state of the amino version has also been extensively exploited in the development of "off−on" switches and

sensors.[59−61] However, their biological profiling has demonstrated that minor structural changes can have a significant impact on their biological properties. Hence, with this is mind, we set about developing another family of ruthenium(II) 1,8-naphthalimide conjugates by (a) modifying the structure from a para-substituted "linear" arrangement to a meta-substituted "wedged" orientation and (b) replacing the bipyridine ligand with the 1,4,5,8-tetraazaphenanthrene (TAP) ligand (Figure 1, **1** and **2**), which become highly oxidizing upon visible excitation.[62,63] These modifications were expected to effect increased DNA binding affinity and DNA photocleavage efficiency by placing the metal center and activated TAP ligands in the optimal positions to ensure a tight fit in the DNA helix.

Herein we report our findings where we have synthesized four novel ruthenium(II) 1,8-naphthalimide conjugates **1−4** (Figure 1). As eluded to above, it was expected that the 1,8-naphthalimide would contribute to high-affinity DNA binding through intercalation, while the Ru(II) center should contribute to the interaction through electrostatic association with the double helix or insertion into the grooves of DNA. Our design would make use of a rigid aromatic group as the linking moiety, allowing for control of the orientation of the components of the complex with respect to each other, where a meta arrangement around the connecting ring with respect to the Ru(II) center was chosen to compare the binding affinities with those of previously reported structures **5** and **6** and to investigate the effect of substitution on their DNA binding

Scheme 1. Complexation of Ligand 7 with Ru(TAP)₂Cl₂ and Reduction of the Resulting Complex[a]

7   1   2
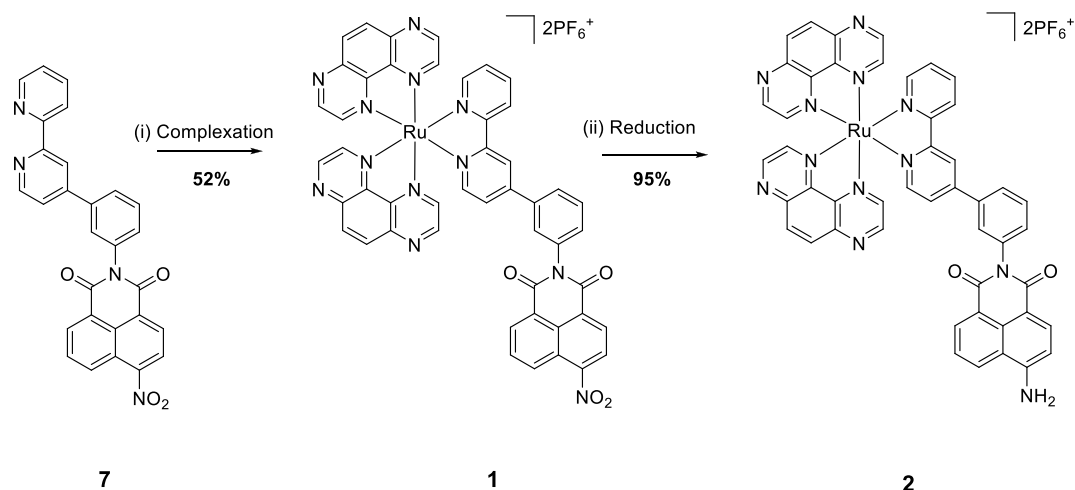
[a]Reagents and conditions: (i) Ru(TAP)₂Cl₂, DMF/H₂O, argon; (ii) MeOH, Pd/C, 1 atm of H₂.

(a)   **(b)**
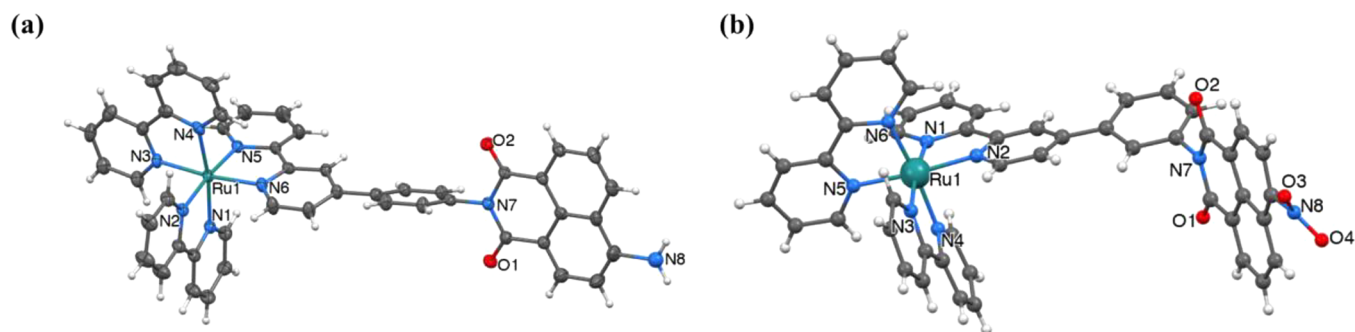

Figure 2. (a) View of the molecular structure of the cation of **6**. Interstitial CH₃CN molecules and PF₆⁻ are removed for clarity and ellipsoids shown at 50% probability. (b) Ball-and-stick representation of the cation of **3** as determined by crystallography.

affinity. In addition, the attached 1,8-naphthalimide structures should serve to further increase the excited-state reactivity, while simultaneously providing a known set of photophysical properties that could be used to monitor the binding process. For compounds **1** and **2**, it was expected that the inclusion of two TAP ligands in their design would serve to increase the DNA cleavage efficiency of these systems and, moreover, to provide a direct comparison between the Ru(bpy)₂(L) and Ru(TAP)₂(L) systems (L = bipyridine−1,8-naphthalimide conjugate).

■ RESULTS AND DISCUSSION

Synthesis of Napthalimide−Polypyridine Ligands and Ruthenium(II) Complexes. The formation of the complexes **1−4** involved the synthesis of the conformationally restricted bipyridine-1,8-naphthalimide ligand **7**, which was synthesized according to a modified procedure originally reported by Johansson et al.[64] (see the Supporting Information), before reaction with Ru(bpy)₂Cl₂ or Ru-(TAP)₂Cl₂ using a N,N-dimethylformamide (DMF)/water (H₂O) mixture was conducted under microwave-assisted conditions. This yielded **1** in 52% yield and **3** in 75% yield after purification using (flash) column chromatography, followed by counterion exchange and crystallization (see the Experimental Section and further details in the Supporting Information). Reduction to the corresponding 4-amino-1,8-naphthalimide analogues **2** and **4** was successfully achieved in

95% and 98% yield, respectively, using Pd/C under a H₂ atmosphere (exemplified in Scheme 1 for **1** and **2**). Synthesized as their chloride salts by stirring a solution of the complexes in methanol (MeOH) with an Amberlite ion-exchange resin, **1−4** were fully water-soluble. The successful synthesis of compounds **1−4** was confirmed by ¹H and ¹³C NMR, high-resolution mass spectrometry (HRMS), and elemental analysis (see below and the Supporting Information for further details). The ¹H and ¹³C NMR spectra showed well-resolved resonances for the polypyridyl as well as naphthalimide components. HRMS showed the expected isotopic distribution patterns, and elemental analysis confirmed that the complexes were obtained as pure materials. Moreover, as stated above, complexes **5** and **6** had previously been developed in our laboratory and were remade for comparison purposes here. Their characterization matched that of our previously published work.[53]

In the case of **3** and **6**, crystals that were found to be suitable for X-ray diffraction analysis were grown upon slow evaporation. Unfortunately, the data set collected for **3** was of poor quality and only allowed for connectivity to be established. Small red platelike crystals of **6** were obtained by evaporation from acetonitrile (MeCN), and the low-temperature (117 K) structure was determined. The structure of **6** is shown in Figure 2a, having crystallized in the triclinic space group P1̄ and containing one molecule of **6**, one full occupancy, and a half-occupancy interstitial CH₃CN molecule

in the asymmetric unit. The Ru(II) center in **6** is coordinated by two unsubstituted 2,2′-bipyridine molecules and one molecule of **7**, giving an overall N6 coordination sphere that adopts a distorted octahedral geometry ($S = 71°$). Bond lengths [2.068(5)−2.085(5) Å] and angles [cis bond angles = 78.9(2)−97.4(2)°; trans bond angles = 171.1(2)−174.1(2)°] to the Ru(II) center are typical for RuN6 complexes. The solvent mask routine in *OLEX2* was required to mask the electron density from one severely disordered PF_6^- counteranion. The amino group attached to the 4 position of 1,8-naphthalimide is disordered over two sites with relative occupancies of 0.65 and 0.35 (a common feature for 4-substituted 1,8-naphthalimide compounds). The ability of naphthalimide groups to be involved in π-based interactions is well-known, and within this complex, the naphthalimide moiety is involved in a strong anion⋯π interaction with the PF_6^- counterion (centroid⋯F2 = 3.322 Å). Interestingly, unlike other naphthalimide-containing complex structures,[65,66] no immediately obvious structure extension influences (e.g., π−π stacking between neighboring complexes, formation of π-stacked layers, etc.) are arising from the naphthalimide moiety. Small, poor-quality crystals of **3** were obtained as red blocks; however, the diffraction data were not of sufficient quality to allow anything other than atom connectivity to be reported. The connectivity is similar to that of **6**, where the Ru(II) center is coordinated by two unsubstituted 2,2′-bipyridine molecules and one molecule of **3**, giving an overall N6 coordination sphere with octahedral geometry (Figure 2b).

Photophysical Characterization. Having successfully synthesized the Ru(TAP)$_2$ complexes **1** and **2** and the Ru(bpy)$_2$ complexes **3** and **4**, their spectroscopic properties were investigated in 10 mM phosphate-buffered aqueous solutions at pH 7.4. Examination of the UV/vis absorption spectrum of **1** (Figure 3a) revealed absorption bands characteristic of both the ruthenium(II) polypyridyl and 4-nitro-1,8-naphthalimide chromophores, where the intense band centered around 275 nm was attributed to π−π* intraligand transitions, the band at 358 nm to the 1,8-naphthalimide π−π* transitions, and the band centered at 415 nm to the metal-to-ligand charge-transfer (MLCT) transitions of the ruthenium(II) polypyridyl center. Similar bands were observed for **3** at 287, 351, and 457 nm, respectively. Each complex displayed two MLCT transitions that are similar to their parent complexes Ru(TAP)$_2$(bpy)$^{2+}$ (412 and 465 nm) and Ru(bpy)$_3^{2+}$ (424 and 452 nm) (see the Supporting Information).[67] Notably, bands characteristic of 1,8-naphthalimide and Ru(II)-based MLCT were resolved. This is important because it allows for direct addressing of both parts of the complex in a semiselective manner, and as such, this is a useful property to examine the interaction and contribution of both components upon binding of the complexes to DNA. The absorption properties of the amino derivative Ru(TAP)$_2$ complex **2** were shown to be somewhat different from those of **1** (Figure 3b). The band at 275 nm was still present, although its molar absorptivity was slightly increased; a broad band was observed at 425 nm corresponding to both the 4-amino-1,8-naphthalimide and Ru(II)-based MLCT transitions.

Complex **4** showed behavior similar to that observed for **2**, with slightly shifted maxima at 287 and 451 nm (see the Supporting Information). A summary of the absorption properties of **1**−**4** is given in Table 1.
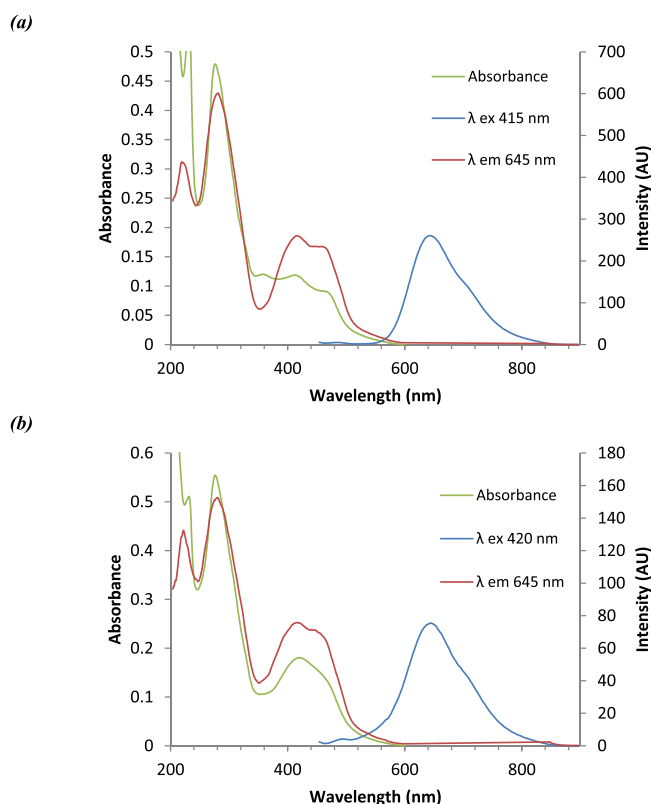

Figure 3. UV/vis absorption and fluorescence excitation and emission spectra of (a) **1** and (b) **2** (10 μM) in 10 mM phosphate buffer at pH 7.4.

In the case of the 4-nitro-1,8-naphthalimide-containing complexes **1** and **3**, excitation of the naphthalimide absorbance bands did not yield naphthalimide-based emission but resulted in MLCT-based emission at 645 and 625 nm, respectively, which is similar to that observed for the parent complexes, Ru(TAP)$_2$(bpy)$^{2+}$ (649 nm) and Ru(bpy)$_3^{2+}$ (617 nm).[67] The absence of 1,8-naphthalimide-associated emission suggested that sensitization of the MLCT excited state occurred through an energy-transfer process, in a manner similar to that of complexes that we have previously described.[68] The MLCT origin of emission for **1** was confirmed by the excitation spectrum recorded for the emission at 645 nm (Figure 3a, red trace), where, in contrast to the absorption spectrum, there is an absence of the naphthalimide band. Excitation of **2** and **4** at 425 or 450 nm resulted in similar behavior, in that no emission was observed from 1,8-naphthalimide, with emission bands centered at 645 and 625 nm for the MLCT emission. The MLCT origin of emission was also confirmed for **2** by the excitation spectra recorded for the emission at 625 nm, which closely mirrored the absorption spectrum (Figure 3b, red trace). This again demonstrates a very efficient energy transfer from the naphthalimide excited state to the Ru(II)-based MLCT state. The Φ_F value for **1** was found to be 0.022 (±10%), which is approximately half that reported for [Ru(TAP)$_2$(bpy)]$^{2+}$ but higher than that reported for the Ru(bpy)$_2$ analogue **3**, which exhibited a value of 0.001.[67,68] Conversely, the Φ_F value for **2** was found to be 0.004 (±10%), a value lower than that described for its Ru(bpy)$_2$ analogue **4**, which was reported as 0.018. The reduction in the quantum yields, and the resulting weak emission displayed by these complexes, is attributed to an interaction between 1,8-

Table 1. Absorption and Emission Properties of 1−4 in Aerated 10 mM Phosphate Buffer, at pH 7.4, at 298 K

| | λ_{max} (nm) [ε (M^{-1} cm^{-1})] in phosphate buffer (±10%) | | | | | |
complex	$\pi-\pi*$ IL	$\pi-\pi*$ Naph	MLCT	$\lambda_{emission}$ (nm)	Φ_f (±10%)	τ_{em} (ns) (air)
1	275 [61250]	358 [15300]	415 [15000]	645	0.022	437
2	275 [65700]		425 [22900]	645	0.004	166
3	287 [78159]	351 [18787]	457 [14765]	625	0.001	
4	287 [53055]		451 [17502]	625	0.018	

naphthalimide and the MLCT triplet state. Similar phenomena have been observed for Ru(TAP)$_2$−aminoquinoline conjugates and were attributed to electron-transfer processes between the Ru(TAP)$_2$ center (chromophore) and organic moiety (quencher).[69]

We anticipate that a similar process is likely to be occurring here, where the excited state of the metal complex is efficiently quenched by electron transfer to the 1,8-naphthalimide moiety. Interestingly, the quantum yield of amino-substituted 2 is greatly reduced in comparison to the nitro derivative 1, suggesting that aminonaphthalimide is a more efficient quencher than its nitro counterpart in the case of the Ru(TAP)$_2$(bpy) systems. Conversely, for the Ru(bpy)$_3$ complexes, the quantum yield of amino-substituted 4 is greater than the nitro derivative 3, suggesting that 4-nitro-1,8-naphthalimide is a more efficient quencher than its amino analogue in this instance. Excited-state lifetime measurements (τ_{em}) followed the same trend, where 1 and 2 showed τ_{em} values of 437 and 166 ns, respectively, with the lower τ_{em} value being exhibited by 2 because of its ability to efficiently quench the MLCT-based emission. The main difference in the emission properties between the bpy- and TAP-based complexes originates from the difference in the level of bpy and TAP $\pi*$ orbitals. The TAP $\pi*$ orbital is lower in energy than that of the bpy ligand.[67] This leads to the TAP complexes being highly oxidizing in their excited state, inducing an efficient electron transfer from aminonaphthalimide. The variation in the reduction potential of 4-amino-1,8-naphthalimide (more easily oxidized) compared with the 4-nitro species results in more efficient quenching of the excited state by 4-aminonapthalimide by electron transfer, thus resulting in an increased fluorescence quantum yield being displayed by 1. The λ_{max}, τ_{em}, and Φ_F values for 1−4 are summarized in Table 1.

DNA Binding Studies: Absorption Titrations. On the basis of our previous work on Ru(bpy)$_3$−4-nitro- and −4-amino-1,8-naphthalimide conjugates, it was expected that 1−4 would interact strongly with DNA, resulting in significant modulations of their photophysical properties.[53] Due to their bifunctional nature, it was also expected that the complexes would interact with DNA through a combination of electrostatic and π-stacking interactions, where the metal complex should bind externally to the phosphate backbone, while the 1,8-naphthalimide moieties would bind through intercalative or groove binding interactions. To determine the nature of their binding affinity for DNA, UV/vis absorption spectroscopy was first utilized to probe the interaction of 1−4 with DNA. Titrations were carried out by the addition of small aliquots of stDNA to a 10 mM phosphate buffer solution of each complex at pH 7.4, until a plateau in the absorbance was reached. Changes in the ruthenium(II) complex ^{3}MLCT band and in the 1,8-naphthalimide $\pi-\pi*$ band were monitored for 1 and 3, while those changes at the broad band centered at 425 or 451 nm were monitored in the cases of 2 and 4. As representative
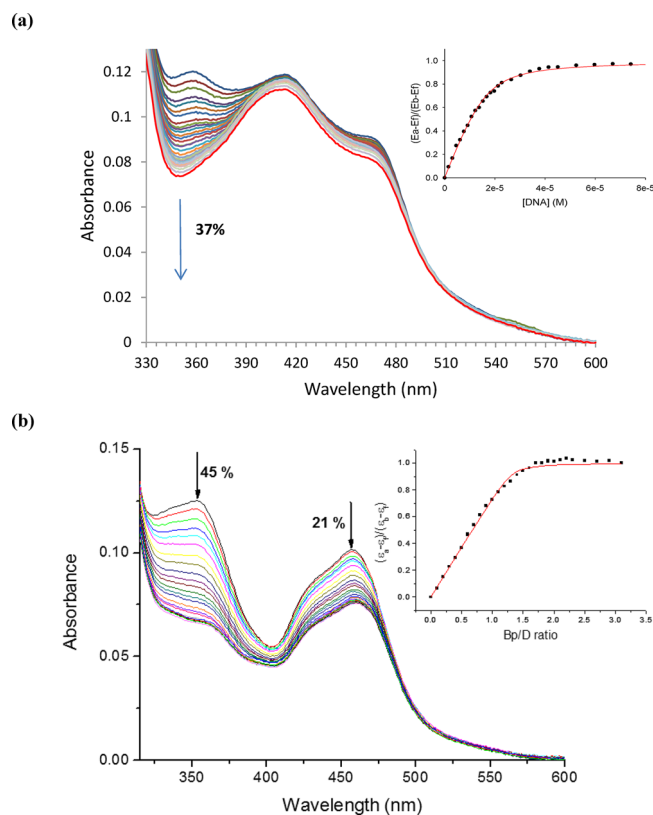

(a)

(b)

Figure 4. (a) Changes in the UV/vis spectrum of 1 (8 μM) with increasing additions of stDNA (0−210 μM). Inset: Plot of ($\varepsilon_a - \varepsilon_f$)/($\varepsilon_b - \varepsilon_f$) versus [DNA] (M^{-1}, P) using data with P/D values between 0 and 12 and the best fit of the data (red ---) using the Bard equation. (b) Changes in the UV/vis spectrum of 3 (6.9 μM) upon the addition of stDNA (0−21.39 μM base pairs). Inset: Plot of ($\varepsilon_a - \varepsilon_f$)/($\varepsilon_b - \varepsilon_f$) versus equivalents of DNA and the corresponding nonlinear fit. All in 10 mM phosphate buffer at pH 7.4.

examples, the changes in the ground state of 1 and 3 are shown in Figure 4 (the results for 2 and 4 are shown in the Supporting Information). The titration of 1−4 with stDNA resulted in significant changes to their absorption spectra. Complex 1 exhibited a 37% decrease in absorbance at 358 nm with a concomitant decrease of 6% in the MLCT band at 415 nm. Similarly, 3 exhibited a 45% decrease in absorbance at 351 nm with a concomitant decrease of 21% in the MLCT band at 457 nm. The absorbance changes displayed by 2 culminated in a 22% decrease in the band centered at 425 nm, while 4 exhibited a 29% hypochromism of the MLCT band. The defined hypochromicities observed in the ground-state spectra of all complexes immediately indicate strong interactions occurring with DNA. In the cases of 1 and 3, the large degree of hypochromicity seen in the $\pi-\pi*$ bands suggests intercalation of the 1,8-naphthalimide moiety between the stacked bases, as expected with such planar structures.

Table 2. DNA Binding Parameters from Fits to Absorbance Data

complex	λ(Naph) hypochromism (%)	λ(MLCT) hypochromism (%)	binding constant K_b (M^{-1})	binding site size n (base pairs)	R^2
1	37	6	1.3×10^6 (± 0.1)	1.3 (± 0.03)	0.99
2		22	5.8×10^6 (± 1.2)	1.5 (± 0.03)	0.99
3	45	21	1.9×10^7 (± 0.6)	1.36 (± 0.02)	0.99
4		29	1.1×10^7 (± 0.5)	1.50 (± 0.06)	0.98
5	34	15	4.5×10^6 (± 0.7)	0.98 (± 0.02)	0.99
6		30	4.5×10^6 (± 0.7)	0.98 (± 0.02)	0.99

Similarly, the changes in the MLCT region confirms that the metal center of **1** and **3** is tightly bound to DNA. Because of the overlap of the MLCT and naphthalimide bands of **2** and **4**, it is more difficult to draw firm conclusions regarding the separate portions of this system. However, the large absorbance decrease observed was also coupled with a slight red shift of the absorbance maxima in both cases, behavior often associated with classical intercalation.[70]

Analysis of the ground-state titration data using the Bard equation[71] confirmed that **1**–**4** show a strong affinity for DNA (summarized in Table 2). Complex **1** showed binding with K_b = 1.3×10^6 (± 0.1) and n = 1.3 (± 0.03), with **2** exhibiting values of K_b = 5.8×10^6 (± 1.2) and n = 1.5 (± 0.03). **3** gave K_b = 1.9×10^7 (± 0.1) and n = 1.36 (± 0.02), while **4** showed K_b = 1.1×10^7 (± 0.7) and n = 1.5 (± 0.06). From UV/vis absorption studies, it is clear that **1**–**4** bind DNA with high affinity, having binding constants on the order of 10^6–10^7 M^{-1}. Furthermore, the nature of the interaction with the binding affinity for DNA appears to be sensitive to the arrangement of the ruthenium(II) and 1,8-naphthalimide components around the connecting ring, where the meta arrangement results in a more intimate association of the Ru(bpy)$_2$ complexes **3** and **4** in comparison to the para derivatives **5** and **6** previously reported [K_b = 4.5×10^6 (± 0.7) and 3.0×10^6 (± 1.0), respectively].[53]

The interaction of **1** and **2** with DNA at varying ionic strengths was also examined using UV/vis absorption spectroscopy, where, at both 50 mM and 100 mM NaCl concentrations, significant spectroscopic changes were also observed. Absorption decreases were observed in all cases (see the Supporting Information) and confirmed retention of a high affinity for DNA, even at very high NaCl concentrations. For example, at 50 mM NaCl, **1** exhibited K_b = 7.4×10^5 (± 0.9), while at 100 mM NaCl, **1** had K_b = 4.3×10^5 (± 1.8). The overall study revealed an expected trend in the binding affinities of these complexes for DNA with K_b at 10 mM phosphate buffer $\geq$ 50 mM NaCl $\geq$ 100 mM NaCl showing an obvious effect of the NaCl concentration on the binding process (a summary of the results obtained are presented in Table S1).

It is well-known that electrostatic DNA binding of ruthenium(II) complexes is dependent on the ionic strength of the medium.[72] Under high salt conditions, we have observed a decrease in the binding strength relative to that in 10 mM phosphate buffer alone; nevertheless, because **1** and **2** retain a high affinity for DNA, even in 100 mM NaCl solution, it can be concluded that, although electrostatic interactions have a role to play in the binding process, it is the bifunctional nature of these systems comprising an intercalating 1,8-naphthlimide and a cationic Ru(II) center that governs the overall association of these complexes with DNA. Previously reported ruthenium(II) complexes that also display both electrostatic

and intercalative interactions with DNA exhibit binding constants of a similar order of magnitude.[37,51,52]

DNA Binding Studies: Emission Dependence Titrations at Low Ionic Strength. In order to further confirm this interaction and monitor any excited-state redox processes, the excited-state properties of **1**–**4** were also monitored as a function of added DNA. As expected, the emission spectra of all complexes studied were found to change dramatically in the presence of increasing concentrations of DNA; however, the results observed differed significantly in each case. The MLCT-based emission of **1** in aqueous solution was shown to undergo excited-state quenching, with a ca. 30% decrease being observed upon the addition of stDNA (P/D of 0 $\rightarrow$ 30), with the main changes occurring at P/D of 0 $\rightarrow$ 3. Similarly, **2** was also shown to have its MLCT-based emission quenched but to a larger degree showing quenching of ca. 43% upon the addition of stDNA (P/D of 0 $\rightarrow$ 30), with the main changes occurring between a shorter P/D range of 0 $\rightarrow$ 2 (see the Supporting Information).

The observed quenching of the excited state is most likely due to photoelectron transfer between *guanine* residues and the ^{3}MLCT state of the complexes, as previously described for systems containing two or more TAP ligands.[73] A biphasic binding profile with an immediate fluorescence decrease followed by a more gradual increase to a plateau over a P/D range of 3 $\rightarrow$ 30 was observed for both complexes, which suggests that these complexes distribute themselves differently on the polynucleotide depending on the availability of binding sites. The extra enhancement of luminescence quenching might originate from DNA-induced stacking of the complexes.[74] For comparison, the emission profiles for each of the systems, **1** and **2**, are shown in the Supporting Information, demonstrating the greater emission modulation experienced by **2** upon titration with DNA. This observation correlates well with the results seen with the UV/vis absorption studies and further reflects the high DNA binding affinity of this system.

In a manner similar to that of the Ru(TAP)$_2$(bpy) complexes, both Ru(bpy)$_3$ complexes **3** and **4** underwent two distinct phases of change in their emission profiles. **3** underwent an initial rapid decrease in the emission intensity over a P/D range of 0 $\rightarrow$ 2 followed by a more gradual increase to a plateau (P/D of 2 $\rightarrow$ 45), while the amino-functionalized complex **4** also experienced two distinct phases of change. The first region in a P/D range of 0 $\rightarrow$ 2 is steep and represents most of the intensity change before becoming more gradual, reaching a plateau at approximately P/D = 30 with an overall 2.6-fold emission enhancement. This enhancement is likely due to tight binding of 1,8-naphthalimide, which holds the metal center in close proximity to the DNA, with subsequent loss of quenching. Interestingly, the emission changes displayed by complex **4** were significantly greater than those for its previously reported analogue **6**.

The increased enhancement that occurs for this system is exemplified in Figure 5, where the emission profiles of both
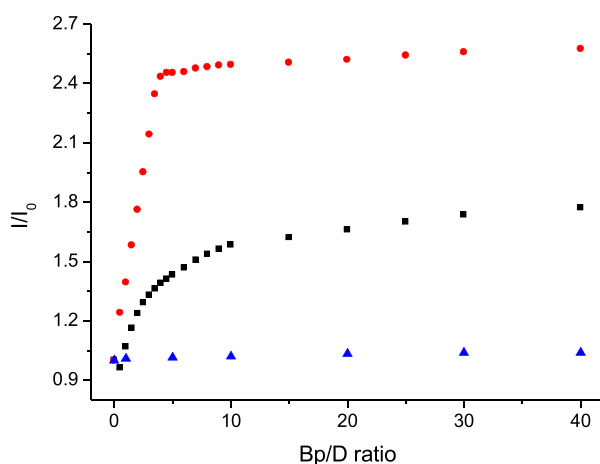

Figure 5. Comparison of the emission intensity changes for Ru(bpy)$_3$$^{2+}$ (blue ▲), **4** (red ●), and **6** (black ■) upon the addition of DNA in 10 mM phosphate buffer at pH 7.4.

complexes are compared with that of Ru(bpy)$_3$$^{2+}$. This greater enhancement may be related to the arrangement of the constituents of the complex around the connecting ring. A meta arrangement creates a cleft, the result of which renders the shape of the complex more complementary to that of DNA. Upon insertion of 1,8-naphthalimide into the helix, the Ru(II) center in **4** is held more tightly bound to the DNA backbone than that in **6** and, as a result, is more effectively protected from quenching. This result suggests that the meta arrangement of the connecting ring in the bpy−1,8-naphthalimide ligand is optimal to ensure a tight binding of the Ru(II) metal center to the DNA backbone.

DNA Binding Studies: Emission Dependence Titrations at High Ionic Strength. The susceptibility of the DNA binding affinity of **1** and **2** to the ionic strength was also investigated by fluorescence titrations at varying concentrations of NaCl (50 and 100 mM), and as seen above from UV/vis absorption titrations, the overall emission modulations upon the addition of DNA decrease as a function of added NaCl. Salt back-titrations were carried out to exemplify the effect of increasing NaCl concentration (see the Supporting Information). The fluorescence emission was seen to be affected by increasing NaCl concentration, gradually increasing toward that of the free compound but reaching a plateau at ca. 140 mM NaCl, with about a 40% increase toward that of the free species. No further changes occurred with the addition of up to 250 mM concentration of NaCl, indicating that the majority of the compound remains bound even at high ionic strength. These results give further confirmation that the DNA binding strength is dependent on the ionic strength of the medium for complexes of this type, but even at very high NaCl concentrations, the complexes were not fully displaced; this is most likely due to 1,8-naphthalimide providing high affinity binding through intercalation into DNA.

DNA Binding Studies: Polynucleotide Binding. Studies were also performed with synthetic polynucleotides, [poly(dAdT)]$_2$ and [poly(dGdC)]$_2$, in order to investigate whether any sequence-specific binding could be observed. The interaction of **1** and **2** with both [poly(dAdT)]$_2$ and [poly(dGdC)]$_2$ was measured first using UV/vis absorption

as described above, where a range of values were obtained for K_b from fits to the absorbance data (Table S2). The results highlighted that **1** and **2** exhibited strong binding affinity for both [poly(dAdT)]$_2$ and [poly(dGdC)]$_2$, as observed for stDNA, but no major preference for either was observed (see the Supporting Information).

The excited-state interactions of **1** and **2** with the homopolymers were also monitored and saw substantial differences between [poly(dAdT)]$_2$ and [poly(dGdC)]$_2$, where the characteristic ^{3}MLCT emission bands centered at 645 nm were seen to experience an overall increase upon the addition of [poly(dAdT)]$_2$, while, conversely, the emission was seen to be effectively quenched in the presence of [poly(dGdC)]$_2$. For comparison, the emission profiles for **1** in the presence of stDNA, [poly(dAdT)]$_2$, and [poly(dGdC)]$_2$ are shown in Figure 6.
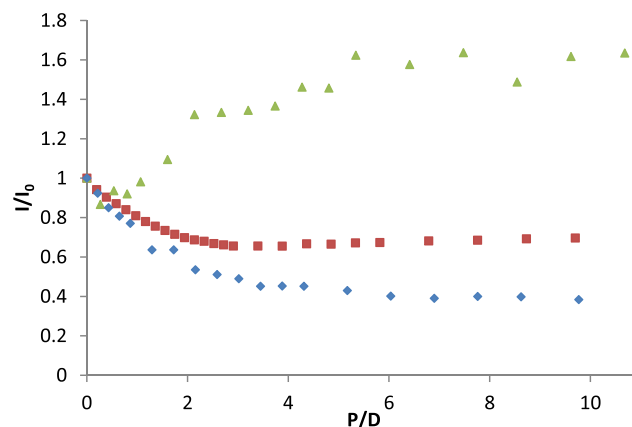

Figure 6. Relative changes in the integrated emission intensity of **1** (8 μM; λ_{ex} 415 nm) with increasing concentrations of stDNA (red ■), [poly(dAdT)]$_2$ (green ▲), and [poly(dGdC)]$_2$ (blue ◆) in 10 mM phosphate buffer at pH 7.4.

For **1** in the presence of [poly(dAdT)]$_2$, an initial slight decrease in emission was followed by a sharp 56% increase culminating in a plateau at $P/D = 10$, while upon titration with [poly(dGdC)]$_2$, the emission was efficiently quenched by 62% at $P/D = 10$. Similarly, in the case of **2** upon titration with [poly(dAdT)]$_2$, the observed fluorescence at 645 nm was seen to experience an initial slight decrease followed by a subsequent 5% overall increase, with the main changes occurring at P/D of $0 \rightarrow 4$. In a manner similar to that of **1**, upon the addition of [poly(dGdC)]$_2$, **2** was shown to have its excited state effectively quenched by 54%, with the main changes occurring at P/D of $0 \rightarrow 2$. As previously mentioned, because of the π-deficient nature of the Ru(II) cores of **1** and **2**, the observed quenching of the ^{3}MLCT states upon the addition of stDNA is expected to be as a result of photoinduced electron transfer reactions with *guanine* nucleobases, a well-documented behavior of complexes containing at least two TAP ligands.[73,75,76] The observed luminescence enhancement in the presence of [poly(dAdT)]$_2$ for both **1** and **2** most likely results from shelter from nonradiative deactivation processes of the ^{3}MLCT excited state afforded by the double-helix microenvironment.[77]

DNA Binding Studies: Thermal Denaturation Studies. Given the above spectroscopic results, thermal denaturation studies were also carried out on **1−4** in order to further elucidate the interaction of these complexes with DNA. In the
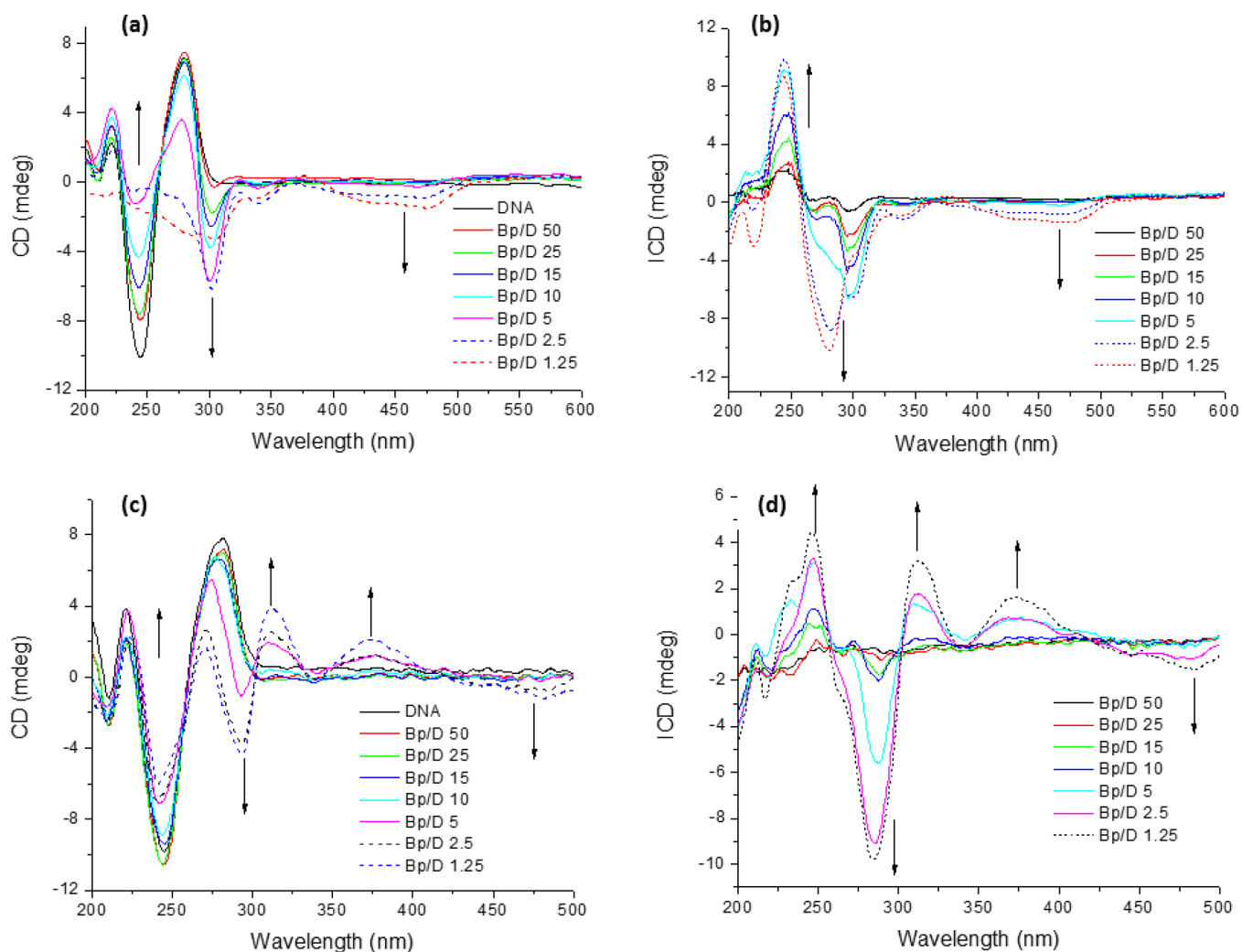
Figure 7. CD curves of (a) ct-DNA (150 μM) in 10 mM phosphate buffer at pH 7, in the absence and presence of **3** at varying ratios and (b) the difference spectra obtained. (c) ct-DNA (150 μM) in 10 mM phosphate buffer at pH 7, in the absence and presence of **5** at varying ratios and (b) the difference spectra obtained.

absence of a ruthenium(II) polypyridyl complex, the T_m value for DNA was determined to be 68 °C, and in all cases, the melting transition for DNA in the presence of the complexes showed large perturbations at all P/D ratios evaluated (see the Supporting Information). The changes reflected stabilization of the helix structure as a function of the complex concentration. At P/D = 25, 10, and 5, the melting transition had not gone to completion at 90 °C, and, consequently, it was not possible to fit the data to a sigmoidal function and, as such, exact melting values could not be reported but may be regarded as being greater than 75 °C. It is noteworthy that the amino complex **2** resulted in a slightly greater stabilization of DNA compared with complex **1**. This result is complementary to those results from the UV/vis absorption and emission studies and emphasizes the higher affinity of **2** in comparison to the nitro analogue **1**.

The different extents of DNA stabilization between the linear and wedged systems were also demonstrated with these experiments. The nitro complex **3** resulted in a significantly greater shift to higher temperature in the melting profile compared with its linear analogue **5**, while the shifts of the amino derivatives **4** and **6** to DNA were less obvious. However, in both cases, the wedged systems result in greater DNA

stabilization than the linear analogues. This result is complementary to those from the UV/vis absorption and emission studies and emphasizes the importance of this minor structural modification, from a linear to a wedged orientation, where the arrangement of the ruthenium(II) and 1,8-naphthalimide components around the connecting ring has a profound effect on the DNA binding affinity.

DNA Binding Studies: Circular (CD) and Linear Dichroism (LD). CD titrations were carried out on Ru(bpy)$_2$ complexes **3−6**, in order to further investigate the influence that the arrangement of the ruthenium(II) and 1,8-naphthalimide components around the connecting ring has on DNA binding. The spectra obtained for the nitro complexes **3** and **5** are depicted in Figure 7.

For complex **3**, a small induced circular dichroism (ICD) signal is observed at long wavelength corresponding to the MLCT absorption, in addition to large changes in the DNA region, attributable to both changes in the CD signal of the DNA itself and ICD of the metal complex in this region. These results are indicative of association of the metal center in the grooves, which results in an ICD signal.[78] In contrast, no changes were seen for the 1,8-naphthalimide moieties in these complexes. Significantly different CD behavior was exhibited
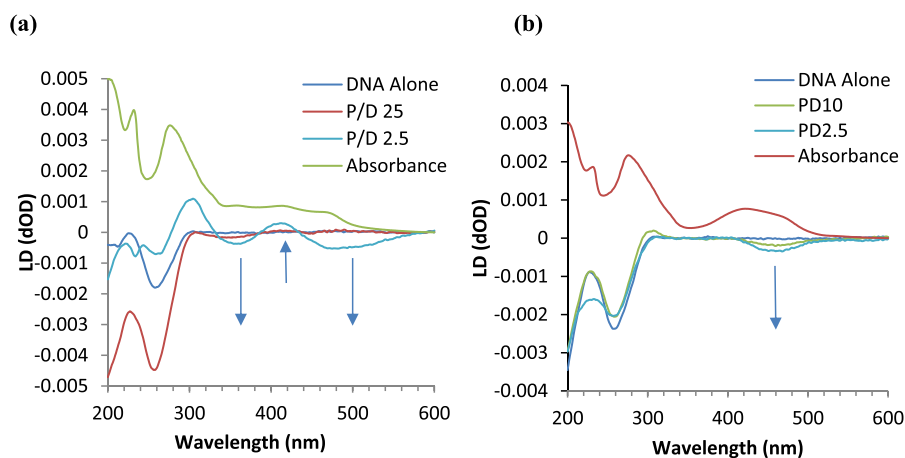
Figure 8. LD spectra of stDNA (150 μM) in 10 mM phosphate buffer, at pH 7.4, in the absence and presence of (a) **1** and (b) **2** at varying ratios.

by the linear nitro complex **5**, where changes at the MLCT band were similar to those observed for **3**. However, these were concomitant with changes in the region of absorption of 1,8-naphthalimide. From examination of the 300−400 nm region, two bands became apparent: a positive signal at 378 nm and a negative signal at 340 nm with a crossover at 355 nm. This type of behavior suggests the formation of dimers or higher-order complexes by stacking in the grooves or externally to the double helix. Such results have previously been observed for species such as methylene blue.[79] It is likely that the absence of CD signals in this region for complex **3** is due to the different orientations of the 1,8-naphthalimides when stacked within the DNA helix. The two amino derivatives **4** and **6** displayed CD behavior similar to each other, where the most significant feature observed was growth of a band in the region of absorption of the metal center. Large changes were also observed in the region of absorption of DNA. The overall results point to a binding mode in which the metal center is tightly associated with the helix, thus experiencing its chirality.

LD studies can also provide strong evidence for the binding mode of metal complexes to DNA, and, hence, LD titrations with complexes **1** and **2** were carried out in order to gain better insight into their specific interaction with the DNA helix. Again, the behavior of **1** was of particular interest because it showed distinct absorption bands for the 1,8-naphthalimide and ruthenium(II) polypyridyl portions of the structure. Consequently, it was expected that its LD behavior would give valuable information on the binding geometry of each of the separate functional moieties. The LD spectra resulting from the addition of **1** to stDNA and a comparison with its absorption spectrum are shown in Figure 8a, with those of **2** shown in Figure 8b. Changes are immediately obvious outside of the DNA absorption region in the case of both complexes, further confirming their strong interaction with DNA in addition to giving information on the specific mode of interaction.

In the case of **1**, when stDNA was treated with a low loading of the complex ($P/D = 25$), a small negative signal is evident at ca. 360 nm, suggesting that the 1,8-naphthalimide portion of the complex is lying perpendicular to the DNA helix axis, i.e., is intercalated. This observation is further emphasized upon higher loading of **1** ($P/D = 2.5$), whereby a more strongly negative signal is observed at ca. 365 nm, with the maximum being slightly red-shifted by 5 nm. More complex behavior is seen in the MLCT absorption region of **1**, where the broad

band is seen to be split in two, with a positive band centered at ca. 415 nm and a negative band with a maximum at ca. 475 nm. This behavior would suggest that the positive band at 415 nm is a result of MLCT from the Ru(II) center to the ancillary TAP ligands lying in the grooves of the DNA helix. Conversely, the negative MLCT band at 475 nm may be associated with an MLCT from the Ru(II) center to the bipyridine fragment of the naphthalimide ligand, further confirming the proposed intercalative geometry of the 1,8-naphthalimide portion. Similar behavior was seen for **2**, whereby a negative signal is observed at 460 nm at $P/D = 25$, and this negative band exhibits a further decrease at $P/D = 2.5$. While it is more difficult to draw firm conclusions for **2** because of the overlap of both the 1,8-naphthalimide and MLCT absorption bands, the negative band centered at ca. 460 nm suggests that the 1,8-naphthalimide portion of this conjugate is, again, most likely intercalated between the nucleobases, as was seen for **1**. Considered with the other spectroscopic studies presented so far, it is likely that, in all cases, the DNA binding involves the insertion of 1,8-naphthalimide into the helix, with tight association of the metal center, through external binding or partial insertion into the grooves. The lower affinity observed for the −NO₂-substituted complexes is likely to be due to steric repulsion caused by the nitro group, which can be twisted slightly out of plane because of steric repulsion from the neighboring H atom in the 5 position of the ring system. The resultant diminished planarity makes intercalation or insertion into the DNA helix less favorable for the nitro-substituted species, while the amino-substituted complexes do not experience this type of twisting, and as such its presence may allow for more complete insertion into the helix, resulting in stronger binding affinity.[80]

DNA Photocleavage Experiments of 1−4. Having clearly identified that **1−4** bind avidly to DNA while displaying varying spectroscopic behavior, it was anticipated that each complex, in addition to binding to DNA, may show photoreactivity with the DNA bases, as has previously been observed for **5** and **6** and various other ruthenium(II) polypyridyl complexes.[52,53] In order to probe this behavior, DNA photocleavage experiments were carried out by treating pBR322 plasmid DNA (1 mg/mL) with each of the complexes **1−4** at varying ratios in a 10 mM phosphate buffer solution before exposure to light irradiation. As shown in Figure 9, the presence of Ru(bpy)₃²⁺ ($P/D = 20$) resulted in an increase to 40% open form after irradiation, confirming its effectiveness as
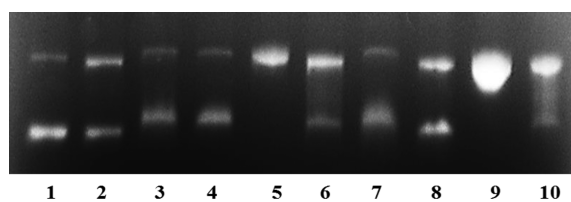
Figure 9. Agarose gel electrophoresis of pBR322 DNA (1 mg/mL) after 30 min of irradiation (2 J/cm^2) in 10 mM phosphate buffer, at pH 7. 4. Lane 1: plasmid DNA control. Lane 2: Ru(bpy)$_3^{2+}$ (P/D = 20). Lanes 3 and 4: **1** and **2** in the dark (P/D = 20). Lanes 5 and 6: **1** and **2** (P/D = 20). Lanes 7 and 8: **3** and **4** (P/D = 20). Lanes 9 and 10: **1** and **2** + NaN$_3$ (P/D 20).

a DNA photocleaver. Importantly, upon incubation in the dark, none of **1**−**4** showed any dark-state DNA cleavage. However, as can be seen in Figure 9, lanes 5 and 6, irradiation and subsequent electrophoresis of pBR322 DNA in the presence **1** and **2** at a P/D ratio = 20 showed clear evidence of efficient DNA photocleavage, with **1** showing complete conversion of the plasmid to open-form DNA and **2** exhibiting an increase in the open form to 75%. Furthermore, compared with the Ru(bpy)$_2$ analogues **3** and **4**, which showed 15% and 48% cleavage, respectively, both **1** and **2** were found to be significantly more effective photocleavage agents. When irradiated in the presence of the known $^1O_2$ scavenger, NaN$_3$ (lanes 9 and 10), it was observed that the photocleavage efficiencies of **1** and **2** were not reduced. The relative amounts of supercoiled versus open-form DNA are summarized in Table S3.

From the above results, it is clear that the Ru(TAP)$_2$(bpy)-1,8-naphthalimide derivatives **1** and **2** display DNA photocleavage with efficiencies greater than those of [Ru(bpy)$_3$]$^{2+}$ and the Ru(bpy)$_3$-1,8-naphthalimide derivatives **3** and **4**. In addition, it appears that the nitro derivative **1** is a more effective photocleaver than its amino-substituted analogue **2**, most likely because of its increased Φ_F value as described above and the opposite trend seen for the Ru(bpy)$_3$-1,8-naphthalimide derivatives. Moreover, the photocleavage efficiencies of **1** and **2** were not affected to any great extent when irradiated in the presence of NaN$_3$, suggesting that $^1O_2$ formation may not be the primary mechanism by which these complexes exert their activity. Detailed biological profiling of **1** and **2** is ongoing and will be presented in a subsequent study; however, given the results presented above, it was of interest to gain further insight into the effect of the arrangement of the ruthenium(II) and 1,8-naphthalimide components around the connecting ring. Thus, below we present more detailed studies carried out on Ru(bpy)$_3$-1,8-naphthalimide derivatives **3**−**6**.

More Detailed DNA Photocleavage Experiments of 3−6. The orientation of the components within these systems was shown to have interesting consequences on the DNA binding behavior; thus, it was expected that this would also be reflected in the cleavage studies. Irradiation of DNA in the absence and presence of each of the complexes, in a 10 mM phosphate buffer solution, showed the nitro-substituted conjugates **3** and **5** displaying poorer photocleavage efficiency than their amino-substituted analogues **4** and **6**. Some minor differences were also apparent between the corresponding linear and wedged derivatives, where slightly greater efficiency was observed in both cases for complexes comprising a linear arrangement of the 1,8-naphthalimide and ruthenium(II) components (e.g., **5** and **6**). Studies carried out in the

presence of the $^1O_2$ scavenger sodium azide (NaN$_3$) showed that the photocleavage efficiency of Ru(bpy)$_3^{2+}$ is almost completely inhibited by the presence of the $^1O_2$ scavenger while the efficiency of the nitro-substituted complex **3** or **5** appeared insensitive to the presence of NaN$_3$, suggesting that damage mediated by singlet oxygen was not important for these derivatives.

The amino-substituted conjugates **4** and **6** were shown to be moderately sensitive to the presence of the singlet oxygen scavenger, with both inducing approximately the same amount of DNA damage in the absence of NaN$_3$, although it was reduced. Nevertheless, in the presence of NaN$_3$, both **4** and **6** still displayed substantially improved cleavage efficiency over the reference Ru(bpy)$_3^{2+}$. To further investigate the involvement of $^1O_2$ in the DNA photocleavage process, studies were carried out in a D$_2$O solution where reactive oxygen species (ROS) has a longer lifetime and would be expected to induce more efficient damage of the DNA. Indeed, as demonstrated in Figure 10, Ru(bpy)$_3^{2+}$ cleavage was observed to be more
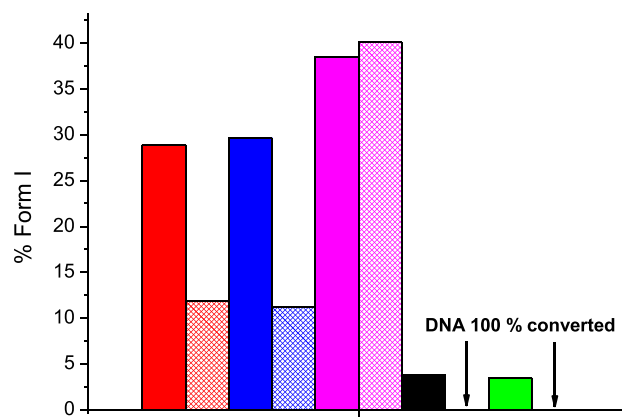

Figure 10. Effect of irradiation in a D$_2$O solution on the photocleavage efficiency of Ru(bpy)$_3^{2+}$ (red ■), **3** (purple ■), **4** (green ■), **5** (blue ■) and **6** (black ■). Solid bars represent cleavage in a H$_2$O solution and hatched bars cleavage in a D$_2$O solution.

efficient in a D$_2$O solution than in a H$_2$O solution. Similarly, complex **5** displayed an enhancement in the photocleavage efficiency in the presence of D$_2$O, implicating $^1O_2$ in the mechanism of damage induced by the complex. This was in contrast to the results obtained with the addition of NaN$_3$ to this system, where no sensitivity to the added $^1O_2$ scavenger was observed. Complex **3** displayed, however, no enhancement in the cleavage efficiency in a D$_2$O solution.

Both **4** and **6** displayed improved photocleavage efficiency of DNA in a D$_2$O solution, giving a quantitative conversion. This, in conjunction with the results in the presence of NaN$_3$, implicates ROS as important reactive species in the damage induced to DNA by these complexes. **4** and **6** displayed significantly greater cleavage efficiency compared with the reference Ru(bpy)$_3^{2+}$, emphasizing the importance of the 1,8-naphthalimide unit in these systems. In summary, the above results demonstrate that complexes **3**−**6** display useful photocleavage properties, whose efficiency depends largely on substitution of the 1,8-naphthalimide moiety; the nitro-substituted complexes **3** and **5** display cleavage efficiencies of the same order as Ru(bpy)$_3^{2+}$. The linear derivative **5** seemed to display some dependence on ROS formation to exert damage, whereas its wedged analogue **3** did not. Both of the
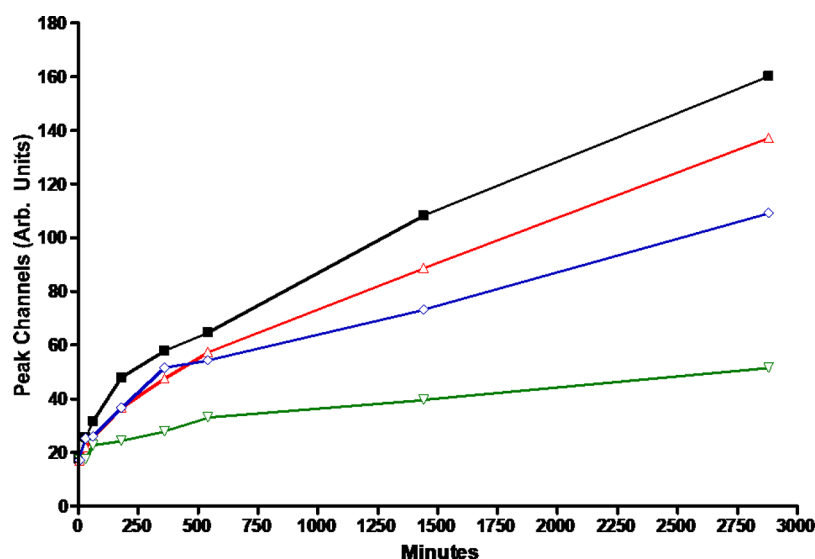
Figure 11. Cellular uptake of **3**−**6** by K562 cells. Cells were treated with **5** (1.0 μM, black ■), **6** (1.0 μM, red ▲), **3** (1.0 μM, green ▽), and **4** (1.0 μM, blue ◆) for various times at 37 °C in the presence of 5% CO_2. Each point at the graph represents a mean from three separate experiments.

amino-substituted complexes **4** and **6** showed improved cleavage efficiency over the reference Ru(bpy)$_3^{2+}$. It was expected that this was due to the high binding affinity of these systems for DNA, which places the metal center in close proximity to the helix, whereby it may effectively induce damage. The damage to DNA caused by **4** and **6** was also shown to involve ROS.

Having investigated the DNA binding and photocleavage properties of **3**−**6** in detail and discovering that the arrangement of the ruthenium(II) and 1,8-naphthalimide components around the connecting ring has a profound effect on the binding mode and affinity, we decided to also undertake an investigation into their biological properties and ascertain whether this small structural modification might also lead to differing behavior in cellulo.

Cellular Uptake Experiments. Cellular uptake is of paramount importance from the point of view of both diagnostics and therapeutics, and, furthermore, access to cellular DNA is important to the viability of **3**−**6** as a new class of PDT agents. Our previous work and the work of others have uncovered the ability of the ruthenium(II) polypyridyl complexes to localize within cancer cells of various types in vitro.[7,26,30,44,81,82] With particular relevance to this study is the observation that ruthenium(II) polypyridyl 1,8-naphthalimide Tröger's bases (themselves synthesized from complexes **4** and **6**) undergo rapid cellular uptake and display intense luminescence inside cells within 2 h of administration.[49] Thus, the ability of **3**−**6** to enter cancer cells was also investigated using a number of techniques.

Flow cytometry was initially used to investigate cellular uptake where both adherent (HeLa) and nonadherent (K562) cells were investigated. **3**−**6** were rapidly internalized by K562 cells, where their fluorescence increased steadily as a function of time (30 min → 48 h). The intracellular fluorescence intensity was shown to increase after 30 min in all cases, with the exception of the wedged nitro derivative **3**. The results also indicated that the wedged derivatives **3** and **4** displayed slower uptake at earlier time points (within 1 h), while cells treated with the linear derivatives **5** and **6** showed a gradual linear increase of fluorescence that was time-dependent (see the Supporting Information). This indicates the importance of the

structural difference between the linear and wedged arrangements in cellular uptake.

As shown in Figure 11, the difference in the emitted fluorescence becomes more evident when the maximum fluorescent intensity is plotted against time, where all complexes were internalized within 9 h. Furthermore, the maximum fluorescence intensity was observed after 24 and 48 h and may be a consequence of high concentrations within the cell or that these compounds are bound to a cellular target.

First, the uptake of each of the complexes into HeLa cells was also verified by flow cytometry studies, where at all time points the amino-substituted complexes **4** and **6** displayed similar intensities, suggesting that the uptake properties of these two derivatives are quite similar in nature. Second, the nitro-substituted complexes **3** and **5** displayed contrasting uptake properties to each other, where the linear derivative **5** was observed to enter cells much more effectively. Complex **5** was found to be the most readily taken up by the HeLa cells after 24 h of incubation. Complex **5** was weakly emissive in solution, possessing a Φ_F value of 0.004 in H_2O, in comparison to the amino complexes **4** and **6**, which possessed Φ_F values of 0.019 and 0.018, respectively. Furthermore, **5** displayed a smaller luminescent enhancement in the presence of DNA than **4** and **6** did. Therefore, for complex **5** to give rise to such a large increase in the fluorescence intensity, it must have been present in the cells at a much higher concentration. The reduced intensity displayed by HeLa cells incubated with **3** may also be reflective of the emission properties of the system; this complex possessed the lowest quantum yield at 0.001. Therefore, the amount of this complex that accumulates in the cells will be approximately the same as that for **5**, with the difference in the intensities resulting from the differing quantum yields of emission possessed by the complexes. Overall, the nitro complexes **3** and **5** appear to enter both K562 and HeLa cells more rapidly than their amino analogues **4** and **6**, but, importantly, these studies showed that each of **3**−**6** can be internalized by both cell types successfully.

Cellular Localization Experiments. Confocal fluorescence microscopy was employed in order to provide visual evidence of the localization of **3**−**6** in HeLa cells. The results obtained are exemplified in Figure 12, which shows the
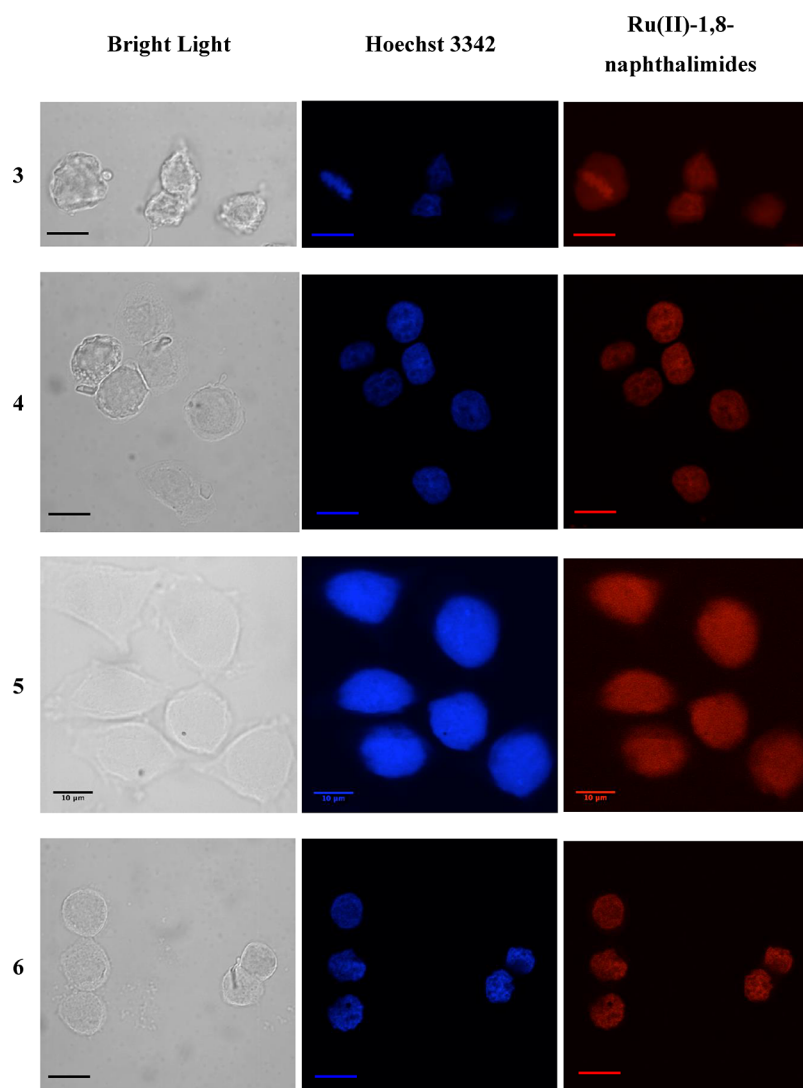
Figure 12. Bright-light and confocal laser scanning microscopy images of HeLa cells treated with **3−6** and stained with Hoechst 3342. Cells were incubated with **3−6** at 10 μM concentration for 24 h before their nucleus was stained with Hoechst 3342 (0.5 μM) for 15 min. The left panel shows the bright-light images of the investigated cells. The middle panel shows the Hoechst 3342 nuclear stain (Ex. 405 nm/Em. 470−500 nm). The right panel shows compounds **3−6** (Ex. 405 nm/Em > 650 nm). Scale bars represent 10 μM.

fluorescence confocal laser scanning microscopy images of HeLa cells after incubation with **3−6**. The observed images show the majority of cells exhibiting intense red fluorescence associated around the nucleus. While a considerable amount of fluorescence arising from **3** was also detected in the cytoplasm, the other derivatives were mainly shown to localize in the nucleus, implied by colocalization staining with the nuclear stain Hoechst 3342. Interestingly, the fluorescence intensities of **1** and **2** measured within the nucleus are somewhat lower in intensity in comparison to that observed surrounding the nuclear membrane. Such behavior may imply the occurrence of photoredox processes between **1** and **2** and the nuclear DNA, causing the emission intensity of these complexes to be effectively quenched, as was observed in vitro during the excited-state DNA titrations (the corresponding images for **1** and **2** are shown in the Supporting Information). In summary, these results indicate that the combination of a ruthenium(II) polypyridyl center with a more lipophilic 1,8-naphthalimide unit is effectively internalized by cells, enabling them to selectively localize inside the nucleus and bind to cellular DNA.

Cytotoxicity and Phototoxicity Studies. In order to investigate the cytotoxic and phototoxic properties of **3−6**, MTT cytotoxicity assays were carried out on K562 cells at various concentrations in both the absence and presence of a varied light dose (2, 4, and 8 J/cm^2). The results of the toxicity studies are shown in Figure 13 and summarized in Table 3.

The wedged 4-nitro derivative **3** showed the highest cytotoxicity in the dark, suggesting that its high DNA binding affinity may give rise to some dark toxicity. **4−6**, however, showed minimal dark toxicity, exhibiting EC$_{50}$ values that were higher than 100 μM. Conversely, as shown in Table 4, the wedged amino derivative **4** displayed the highest phototoxicity with an EC$_{50}$ value of 66.5 μM upon 2 J/cm^2 irradiation. The linear 4-amino derivative also showed a cytotoxicity increase upon irradiation with 2 J/cm^2 (>100 μM $\rightarrow$ 86.5 μM); however, no apparent changes were exhibited upon irradiation with the 4-nitro derivatives **3** and **5**. These results correlated well with the results observed from the DNA photocleavage experiments, where the 4-amino derivatives **4** and **6** showed considerable photocleavage activity.
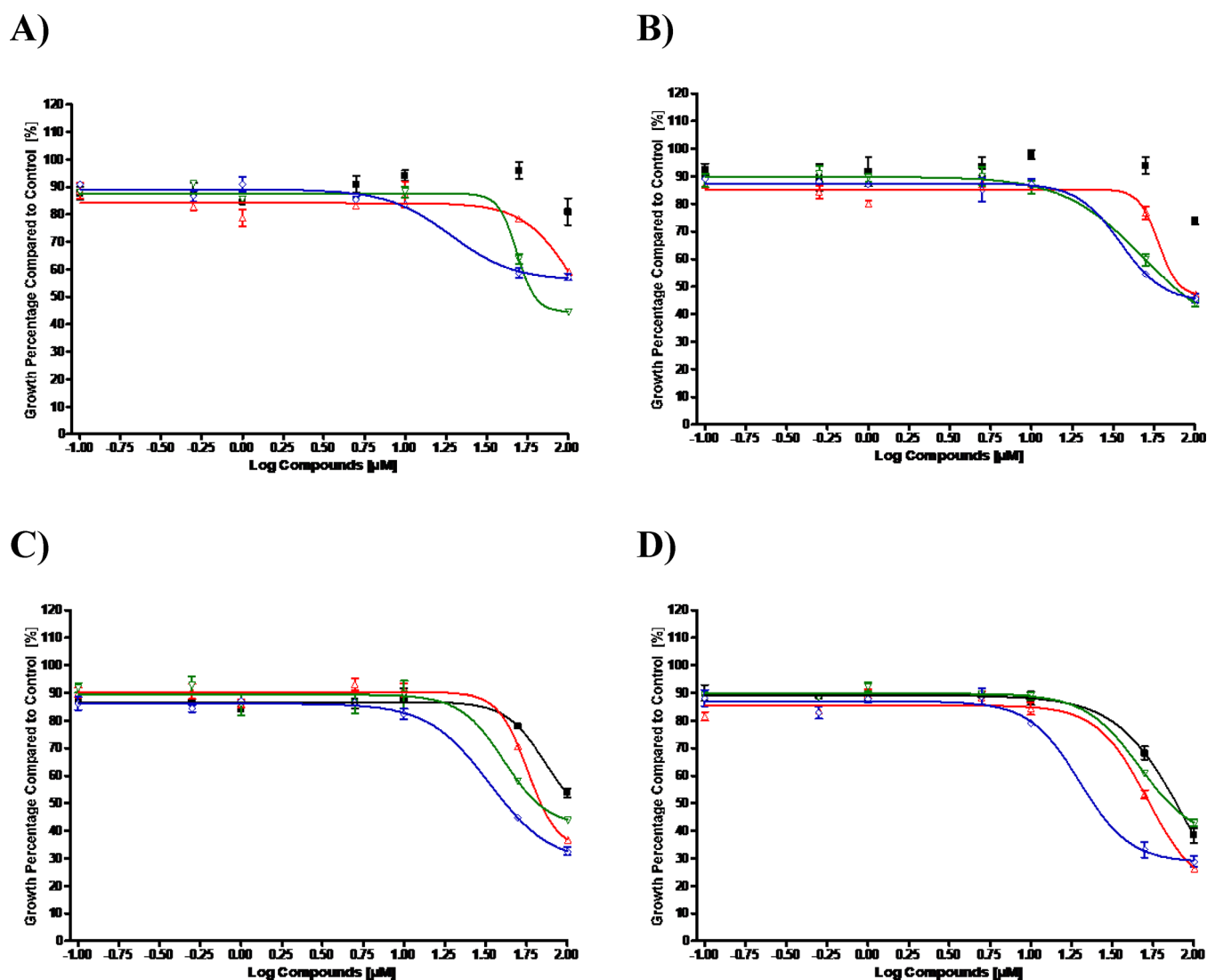
A)

B)

C)

D)

Figure 13. In vitro cyto- and phototoxicity of **3−6** against K562 cells after 24 h of incubation postirradiation: (A) dark controls; (B) 2 J/cm^2; (C) 4 J/cm^2; (D) 8 J/cm^2. Cells were treated with **3** (green ▲), **4** (blue ◆), **5** (black ■), and **6** (red ▼).

Table 3. Summary of EC$_{50}$ Values (μM) for 3−6 after Irradiation with Different Light Doses after 24 h Postirradiation[a]

	3	4	5	6
0 J/cm^2	71.2 ($\pm$6.9)	>100	>100	>100
2 J/cm^2	74.0 ($\pm$7.5)	66.5 ($\pm$9.2)	>100	86.5 ($\pm$8.3)
4 J/cm^2	63.6 ($\pm$9.5)	41.7 ($\pm$2.3)	>100	69.2 ($\pm$3.3)
8 J/cm^2	69.6 ($\pm$8.4)	24.4 ($\pm$3.0)	73.1 ($\pm$4.4)	53.4 ($\pm$4.0)

[a]Each value represents a mean calculated from a single experiment in triplicate ($\pm$SEM).

Table 4. Cell Cycle Analysis of K562 Cells Untreated or Treated with 3−6 and Irradiated with 4 J/cm^2

	NT	NT + Irr	3	4	5	6
sub-G$_1$	5.01 ($\pm$0.3)	5.71 ($\pm$0.4)	5.74 ($\pm$0.1)	10.1 ($\pm$0.1)	8.63 ($\pm$0.4)	8.64 ($\pm$0.3)
G$_1$	52.3 ($\pm$0.6)	48.9 ($\pm$0.6)	46.1 ($\pm$1.0)	40.7 ($\pm$0.4)	40.6 ($\pm$0.4)	32.1 ($\pm$0.4)
S	24.7 ($\pm$0.3)	26.6 ($\pm$0.5)	27.1 ($\pm$0.6)	25.0 ($\pm$0.8)	29.9 ($\pm$0.1)	26.0 ($\pm$0.4)
G$_2$/M	15.6 ($\pm$0.5)	17.1 ($\pm$0.4)	20.9 ($\pm$0.6)	22.4 ($\pm$0.3)	21.2 ($\pm$0.1)	32.0 ($\pm$0.1)

Similar results were obtained with increased light dose, where the phototoxicity was the highest for **4** and **6**, while the 4-nitro derivatives showed a minimal increase even at 8 J/cm^2. These results confirm the light-activated therapeutic potential of **4** and **6**, where the 4-amino derivatives were highly effective against the growth of K562 cells upon photoactivation, particularly with a 8 J/cm^2 light dose.

In order to further probe the mechanism of action of these compounds and to determine whether ROS played a role in their photoactivity, further flow cytometry experiments were
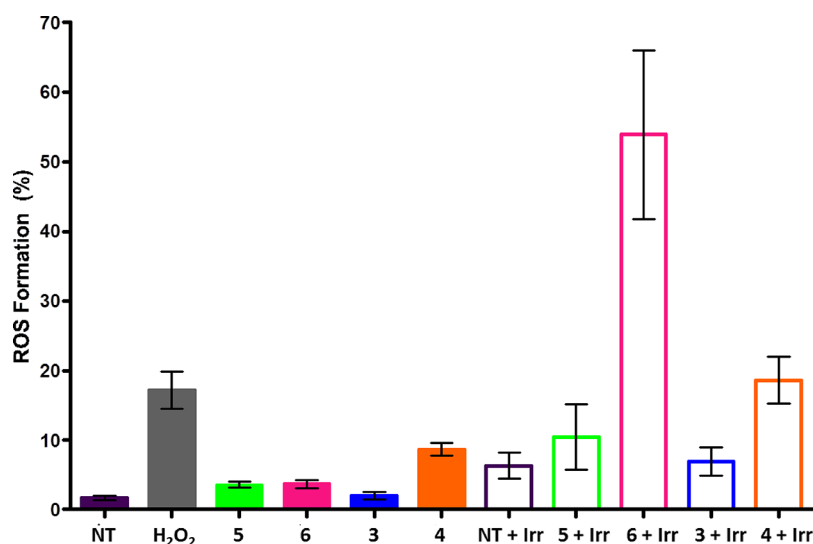
Figure 14. Summary of ROS production in K562 cells after treatment with **3**−**5**. Cells were treated with **5** (10 μM, green ■), **6** (10 μM, purple ■), **3** (10 μM, blue ■), and **4** (10 μM, red ■) for 24 h before they were irradiated (open bars) or left in the dark (solid bars). Vehicle-treated cells (NT) are indicated with purple ■, and cells treated with 2 mM H_2O_2 are represented by a gray ■.
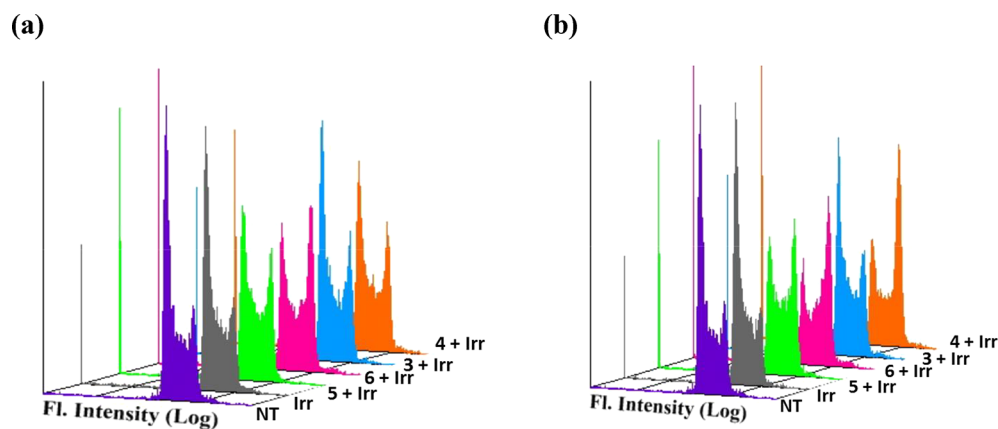

Figure 15. Cell cycle analysis of K562 cells irradiated with (a) 4 J/cm^2 and (b) 8 J/cm^2. Cells were either left untreated (blue ■) or treated with **5** (10 μM, green ■), **6** (10 μM, pink ■), **3** (10 μM, light blue ■), and **4** (10 μM, red ■) for 24 h before irradiation. Cells were analyzed 48 h after irradiation. Untreated, irradiated cells are indicated with a solid gray plot.

conducted to measure the production of ROS arising from cells treated with **3**−**6** both in the dark and after photoactivation. Dihydroethidium (DHEM) was used to investigate the involvement of ROS, where it was expected that the production of ROS would convert DHEM to ethidium, giving rise to increased ethidium fluorescence upon its intercalation into DNA. A summary of the results is shown in Figure 14, where all compounds exhibited a small increase in ROS formation in the dark with the exception of compound **3** despite this being the most cytotoxic compound in the dark, as was discussed above, and indicating that **3** might exert its biological activity through a different mechanism. A minimal increase in ROS formation was observed in untreated cells after 8 J/cm^2 light dose, but, most interestingly, the linear 4-amino derivative **6** showed the highest increase, while the corresponding wedged 4-amino derivative **4** showed the second-highest ROS formation. These results correlate well with the phototoxicity analyses discussed above and may suggest that the phototoxicity exerted by these compounds involves the production of ROS. The 4-nitro derivatives **3** and **5** showed trends similar to those obtained from the

phototoxicity studies, where the linear derivative **5** showed a minimal increase in the cytotoxicity upon irradiation and the wedged 4-nitro derivative **3** showed small or no changes after irradiation. It is clear from the above results that the 4-amino substituents on the 1,8-naphthalimide chromophore are important for ROS production, where they have been shown to have higher fluorescence quantum yields and also higher DNA photocleavage efficiencies.

To further examine the effects of these compounds on cellular DNA, cellular growth, and initiation of apoptosis, a flow-cytometry-based cell cycle analysis assay was also conducted. As shown in Figure 15 and Table 4, irradiation with 4 J/cm^2 light doses leads to a minimal increase in cells that are situated in the G_2/M phase of the cell cycle, indicating that light irradiation promoted DNA damage, resulting in the G_2/M block and activation of the DNA repair mechanism. Furthermore, this light dose was shown to induce apoptosis to a small population of cells that were incubated in the absence of **3**−**6**. However, in the presence of **3**−**6**, cells were arrested in the G_2/M phase to a larger extent than the untreated cells upon irradiation with a 4 J/cm^2 light dose. Furthermore, the
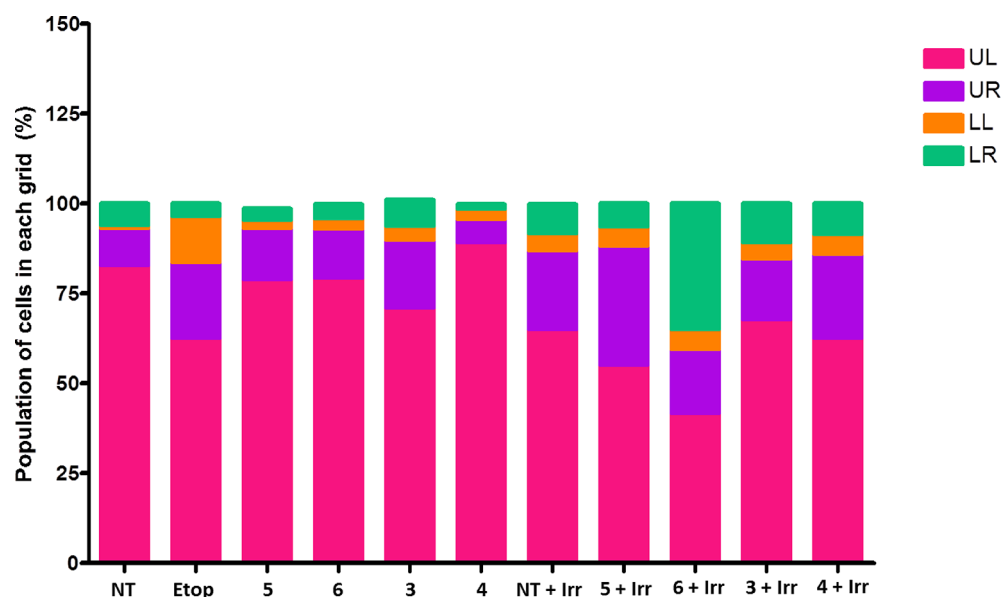
Figure 16. Summary of the results obtained from the flow cytometry analysis of the MMP after treatment with **3−6** in the presence and absence of a 8 J/cm^2 light. UL represents the upper left grid and corresponds to healthy cells. The upper right (UR) grid correlates to cells with partially depolarized mitochondria, and the lower grids (LL and LR) represent cells that exhibited complete loss of the MMP. Each stacked bar corresponds to a mean from two individual experiments.

linear 4-amino derivative **6** induced the highest amount of G$_2$/M blocked cells, correlating well with the previous results. Treatment with **3−6** also showed considerable induction of apoptosis, especially by the wedged 4-amino derivative **4**, which showed 10% apoptosis. An overall trend similar to that for the phototoxicity investigation was obtained, where the 4-amino derivatives **4** and **6** were shown to be more phototoxic than the 4-nitro derivatives **3** and **5**. These results indicate that treatment with **3−6** may cause apoptosis, induced by arresting cells in the G$_2$/M phase of the cell cycle. The G$_2$/M checkpoint has been shown to be activated upon DNA damage, and in light of these results, it is possible that these compounds are responsible for DNA photocleavage within cells. The effects were more pronounced with a 8 J/cm^2 light dose, again indicating that increased light doses give rise to increased toxicity (see the Supporting Information).

The effects of **3−6** on the mitochondrial membrane potential (MMP) was also evaluated using the flow cytometry JC-1 assay, whereby an increase in green fluorescence is an indicator of a loss of MMP.

A summary of the results is shown in Figure 16 with corresponding plots found in the Supporting Information. The results showed that the positive control, etoposide, displayed an induction of cells exhibiting a complete loss of MMP of 30%. The cells that were treated with **3−6** in the dark did not induce any major changes to the mitochondrial potential, although treatment with compound **3** showed an increase in the number of cells with partially depolarized mitochondria compared with the untreated control. These results again agree with the previously discussed cytotoxicity studies, where **3** was found to be the most cytotoxic compound in the dark. However, the MMP was affected upon irradiation with a 8 J/cm^2 light dose. The linear 4-amino derivative **6** showed the highest percentage of cells with a complete loss of the MMP. These results are in agreement with the cytotoxicity and ROS production studies discussed above, where this compound was shown to be the most cytotoxic and induce the highest

percentage of ROS. Furthermore, these results also indicated rapid apoptosis induction by **3** compared with the other complexes. Treatment with **5** upon irradiation resulted in an increase in cells with partially depolarized mitochondria, while the wedged derivatives **3** and **4** showed results similar to those with the irradiated control.

CONCLUSIONS

In conclusion, we have reported the synthesis and photophysical characterization of four new DNA binding ruthenium complexes **1−4** appended with either 4-amino- or 4-nitro-1,8-naphthalimide. A meta arrangement around the ring connecting 1,8-naphthalimide to a bipyridine ligand creates a cleft, the result of which renders the shape of the complex complementary to that of DNA. We have demonstrated that **1−4** show water solubility and a distinctive set of photophysical properties that has allowed the nature of their interaction with DNA to be probed by various ground- and excited-state titrations. From these titrations, DNA binding affinities with stDNA, $[\mathrm{poly(dA\text{-}dT)}]_2$, and $[\mathrm{poly(dG\text{-}dC)}]_2$ have been evaluated as being on the order of 10^6 M^{-1}. Furthermore, given the π-deficient character of **1** and **2**, they have been shown to exhibit highly oxidizing excited states that are effectively quenched by redox interactions with *guanine* sites on DNA. Similarly, the tight binding, typical of intercalative interaction, was also apparent from thermal denaturation studies, where large shifts were observed in the T_m values of stDNA in the presence of **1−4** at various binding ratios. From CD and LD studies, an overall binding mode for conjugates **1−4** with DNA was proposed, in which insertion of 1,8-naphthalimide into the helix occurs with concomitant external association of the Ru(II) center. Because of the excellent DNA binding ability exhibited by **1−4**, their ability to act as DNA photocleavers was also examined, where both **1** and **2** were found to cleave supercoiled DNA with much increased efficiencies compared with the Ru(bpy)$_3$-1,8-naphthalimide analogues **3** and **4**. This is attributed to the

nature of the photoactive TAP MLCT state that yields a strongly oxidizing center TAP$^{\bullet-}$, which because of the affinity of the naphthalimide is located in close proximity to the guanine base.[83] More detailed cellular uptake experiments were carried out on complexes **3−6**, with each complex being found to accumulate in the cytoplasm and nucleus of HeLa cells, showing characteristic red MLCT emission. **3−6** were also chosen to proceed to more detailed biological investigation, where they were shown to induce limited cytotoxicity in the dark but to significantly reduce cell numbers in the culture upon irradiation at 450 nm, suggesting photoactivated cytotoxicity within the cells. Interestingly, the trend obtained for the phototoxicity was in correlation with DNA photocleavage studies, where the 4-amino derivatives **4** and **6** were shown to be the most efficient photocleavers. **6** was shown to induce the highest production of ROS after 8 J/cm^2 irradiation, and cell cycle analysis showed that the complexes induced a G$_2$/M block after irradiation at 8 J/cm^2. A similar trend was observed for the cytotoxicity studies, where the 4-amino derivatives **4** and **6** were shown to be superior to the 4-nitro derivatives **3** and **5**. Finally, the MMP was affected by the photoactivation of compounds **3−6**, where the linear 4-amino derivative **6** again showed the greatest increase in cells that had completely lost their MMP. These investigations have shown the potential of ruthenium(II) 1,8-naphthalimides as PDT agents, and further studies are continuing to investigate the biological profiles of complexes **1** and **2** and to identify suitable candidates to progress to in vivo models.

■ EXPERIMENTAL SECTION

4-[N-(m-Phenyl)-4-nitro-1,8-napthalimide]-2,2′-bipyridine (7). 3-([2,2′-Bipyridin]-4-yl)aniline (0.54 g, 2.17 mmol, 1 equiv) and 4-nitro-1,8-naphthalic anhydride (0.53 g, 2.17 mmol, 1 equiv) were suspended in HPLC-grade ethanol (EtOH; 30 mL), and the mixture refluxed in a pressure tube for 48 h. The reaction mixture was cooled to room temperature before the product was collected by suction filtration and washed with EtOH (30 mL), giving the product as a yellow/brown solid (0.86 mg, 84%). ^{1}H NMR (400 MHz, CDCl$_3$): δ_H 8.92 (d, 1H, J = 8.7 Hz, Ar−H), 8.81 (d, 1H, J = 7.4 Hz, Ar−H), 8.75 (m, 2H, Ar−H), 8.7 (s, 1H, Ar−H), 8.68 (d, 1H, J = 5.0 Hz, Ar−H), 8.46 (m, 2H, Ar−H), 8.05 (t, 1H, J = 7.8 Hz, Ar−H), 7.93 (d, 1H, J = 8.0, Ar−H), 7.84 (t, 1H, J = 8.0 Hz, Ar−H), 7.72 (m, 2H, Ar−H), 7.59 (d, 1H, J = 5.0 Hz, Ar−H), 7.42 (d, 1H, J = 7.5 Hz, Ar−H), 7.32 (t, 1H, J = 6.0 Hz, Ar−H). ^{13}C NMR (100 MHz, CDCl$_3$): δ_C 162.2, 156.3, 155.5, 149.5, 149.3, 148.7, 147.7, 139.5, 136.5, 135.0, 132.5, 129.9, 129.8, 129.7, 129.4, 129.0, 128.6, 127.4, 126.9, 126.5, 123.6, 123.5, 123.4, 122.6, 121.2, 120.9, 118.6. ν_{max}(film)/cm^{-1}: 1717 (−CO−N−CO−), 1524 (C−NO$_2$), 1350 (C−NO$_2$). HRMS(-ES). Calcd for C$_{28}$H$_{17}$N$_4$O$_4$ (M + H): m/z 473.1250. Found: m/z 473.1233.

Ru(4-[N-(m-phenyl)-4-nitro-1,8-naphthalimide]-2,2′-bipyridine)(1,4,5,8-tetraazaphenanthrene)$_2$(PF$_6$)$_2$ (1). 7 (0.104 g, 0.22 mmol, 1 equiv) and Ru(TAP)$_2$Cl$_2$ (0.118 g, 0.22 mmol, 1 equiv) were suspended in DMF/H$_2$O (1:1), and the suspension was degassed by bubbling with argon for 15 min. The reaction mixture was heated at 150 °C for 40 min using microwave irradiation before being allowed to cool and filtered. The solvent from the resulting solution was removed under reduced pressure before redissolution in H$_2$O (5 mL). The PF$_6$ salt of the complex was formed by the addition of a concentrated ethanolic solution of NH$_4$PF$_6$, with the resulting precipitate being collected by centrifugation. The dried solid was redissolved in MeCN before purification by the slow diffusion of diethyl ether into MeCN, giving the product as a red/brown solid (0.140 g, 52%). The crystalline solid was converted to the chloride form of the complex by stirring in MeOH with Amberlite anion exchange resin (Cl$^−$ form) for 1 h. Mp: >250 °C. ^{1}H NMR (600 MHz, CD$_3$CN): δ_H 9.15 (m, 2H, TAP-H), 8.93 (m, 2H, TAP-H),

8.88 (m, 2H, Ar−H), 8.74 (m, 2H, Ar−H), 8.69 (d, 1H, J = 7.92 Hz, Ar−H), 8.66 (m, 4H, TAP-H), 8.51 (d, 1H, J = 7.92 Hz, Ar−H), 8.41 (d, 1H, J = 2.70 Hz, TAP-H), 8.33 (d, 1H, J = 2.46 Hz, TAP-H), 8.15 (m, 4H, 2Ar−H and 2TAP-H), 8.07 (d, 1H, J = 7.98 Hz, Ar−H), 7.94 (s, 1H, Ar−H), 7.84 (t, 1H, J = 7.84 Hz, Ar−H), 7.80 (d, 2H, J = 5.94 Hz, Ar−H), 7.64 (m, 2H, Ar−H), 7.41 (t, 1H, J = 6.12 Hz, Ar−H). ^{13}C NMR (150 MHz, CD$_3$CN): δ_C 164.7, 163.9, 158.1, 157.6, 154.2, 154.1, 151.1, 150.9, 150.5, 150.5, 150.5, 149.8, 149.7, 149.4, 146.6, 146.6, 146.5, 143.3, 143.3, 142.98, 142.95, 140.2, 138.0, 137.6, 133.9, 133.80, 133.79, 133.1, 132.2, 131.6, 131.1, 130.9, 130.6, 130.3, 129.0, 128.9, 128.8, 128.2, 126.0, 125.7, 125.2, 124.6, 124.3, 123.2. ν_{max}(film)/cm^{-1}: 1711 (C=O), 1665 (C=O), 1535 (NO$_2$ stretch), 1355 (NO$_2$ stretch). HRMS(-ES). Calcd for C$_{48}$H$_{28}$F$_6$N$_{12}$O$_4$PRu (M + PF$_6^+$): m/z 1083.1042. Found: m/z 1083.1088.

Ru(4-[N-(m-phenyl)-4-amino-1,8-naphthalimide]-2,2′-bipyridine)(1,4,5,8-tetraazaphenanthrene)$_2$(PF$_6$)$_2$ (2). Ru(4-[N-(m-phenyl)-4-nitro-1,8-naphthalimide]-2,2′-bipyridine)(1,4,5,8-tet-raazaphenanthrene)$_2$Cl$_2$ (0.1 g, 0.081 mmol, 1 equiv) was dissolved in HPLC-grade MeOH (20 mL) and 10% Pd/C added. The reaction mixture was subjected to 3 atm of H$_2$ for 24 h. The reaction mixture was filtered through a Celite plug and the solvent removed under reduced pressure to give the product as a red/brown solid (0.092 g, 95%). The crystalline solid was converted to the chloride form of the complex by stirring a solution of the PF$_6$ salt in MeOH with Amberlite anion exchange resin (Cl$^−$ form) for 1 h. Calcd for C$_{48}$H$_{30}$F$_{12}$N$_{12}$O$_2$P$_2$Ru·2H$_2$O: C, 46.72; H, 2.78; N, 13.62. Found: C, 46.65; H, 2.30; N, 13.15. Mp: >250 °C. ^{1}H NMR (600 MHz, CD$_3$CN): δ_H 9.15 (d, 1H, J = 2.76 Hz, TAP-H), 9.14 (d, 1H, J = 2.70 Hz, TAP-H), 8.93 (d, 1H, J = 2.94 Hz, TAP-H), 8.92 (d, 1H, J = 2.76 Hz, TAP-H), 8.86 (d, 1H, J = 1.74 Hz, Ar−H), 8.74 (d, 1H, J = 8.16 Hz, Ar−H), 8.64 (m, 4H, TAP-H), 8.55 (d, 1H, J = 6.90 Hz, Ar−H), 8.43 (d, 1H, J = 8.88 Hz, Ar−H), 8.40 (d, 1H, J = 2.76 Hz, TAP-H), 8.34 (d, 1H, J = 2.70 Hz, TAP-H), 8.32 (d, 1H, J = 8.32 Hz, Ar−H), 8.15 (m, 3H, 2Ar−H and 2TAP-H), 8.00 (d, 1H, J = 8.70 Hz, Ar−H), 7.94 (s, 1H, Ar−H), 7.76 (m, 4H, Ar−H), 7.66 (dd, 1H, J = 1.98 and 6.12 Hz, Ar−H), 7.56 (d, 1H, J = 7.92 Hz, Ar−H), 7.40 (dt, 1H, J = 1.08 and 5.70 Hz, Ar−H), 6.97 (d, 1H, J = 8.28 Hz, Ar−H), 6.06 (s, 2H, NH$_2$). ^{13}C NMR (150 MHz, CD$_3$CN): δ_C 165.6, 164.8, 158.0, 157.6, 154.1, 154.0, 152.9, 151.0, 150.49, 150.48, 150.46, 149.74, 149.69, 149.4, 149.3, 146.57, 146.55, 146.5, 146.4, 143.31, 143.30, 143.0, 142.9, 140.2, 139.3, 137.1, 134.9, 133.8, 133.8, 133.8, 132.6, 131.4, 131.2, 129.7, 129.3, 128.9, 128.0, 125.8, 125.7, 125.6, 123.8, 123.0, 120.9, 110.8, 109.7. ν_{max}(film)/cm^{-1}: 3356 (aromatic C−H stretch), 1675 (C=O), 1628 (C=O), 1584 (NH bend), 1371 (C−N stretch). HRMS(-ES). Calcd for C$_{48}$H$_{30}$F$_6$N$_{12}$O$_2$PRu (M + PF$_6^+$): m/z 1053.1300. Found: m/z 1053.1266.

Ru(4-[N-(m-phenyl)-4-nitro-1,8-naphthalimide]-2,2′-bipyridine)(bipyridine)$_2$(PF$_6$)$_2$ (3). 7 (0.29 g, 0.62 mmol, 1 equiv) was dissolved in DMF and H$_2$O added until it began to precipitate. A few drops of DMF was added to fully dissolve the ligand, and Ru(bpy)$_2$Cl$_2$·2H$_2$O (0.32 g, 0.62 mmol, 1 equiv) was added. The solution was saturated with argon by bubbling for 10 min. The reaction mixture was heated at reflux under an Ar atmosphere for 24 h. The solvent was removed under reduced pressure, and the resulting residue was redissolved in H$_2$O and filtered. The filtrate was reduced in volume, and to it was added a concentrated aqueous solution of NH$_4$PF$_6$. The resulting precipitate was extracted with CH$_2$Cl$_2$ and dried over MgSO$_4$, and the solvent was removed under reduced pressure. The product was purified by silica flash column chromatography, eluting with 40:4:1 CH$_3$CN/H$_2$O/aqueous NaNO$_3$(sat). The chloride form of the complex was reformed by stirring a solution of the PF$_6$ salt in MeOH with Amberlite ion-exchange resin (Cl$^−$ form) for 1 h, giving the product as a red/brown solid (0.45 g, 75%). Calcd for C$_{48}$H$_{32}$F$_{12}$N$_8$O$_4$P$_2$Ru: C, 49.03; H, 2.74; N, 9.53. Found: C, 48.87; H, 2.90; N, 9.25. Accurate MS. Calcd for C$_{48}$H$_{32}$N$_8$O$_4$Ru (M^{2+}): m/z 886.1590. Found: m/z 886.1614. ^{1}H NMR (CD$_3$CN, 600 MHz): δ_H 8.87 (1H, dd, J = 1.0 and 8.8 Hz, Ar−H), 8.83 (1H, d, J = 1.9 Hz, Ar−H), 8.73 (1H, dd, J = 0.9 and 7.3 Hz, Ar−H), 8.72 (1H, d, J = 8.2 Hz, Ar−H), 8.70 (1H, d, J = 8.0 Hz, Ar−H), 8.57 (1H, d, J = 3.4 Hz, Ar−H), 8.56 (3H, m, 3 × Ar−H), 8.51

(1H, d, J = 7.9 Hz, Ar−H), 8.13−8.05 (7H, m, 7 × Ar−H), 7.95 (1H, t, J = 1.9 Hz, Ar−H), 7.84−7.77 (7H, m, 7 × Ar−H), 7.69 (1H, dd, J = 2.0 and 6.1 Hz, Ar−H), 7.60 (1H, m, Ar−H), 7.46−7.42 (5H, m, 7 × Ar−H). ^{13}C NMR (CD$_3$CN, 150 MHz): δ_C 164.7, 163.9, 158.6, 158.0, 152.8, 152.70, 152.67, 152.6, 151.0, 149.3, 138.8, 138.7, 138.0, 137.9, 133.1, 131.8, 131.5, 131.0, 130.9, 130.5, 130.3, 128.9, 128.7, 128.6, 128.5, 128.2, 125.7, 125.6, 125.3, 125.2, 124.6, 124.3, 122.9. IR ν_{max} (cm^{-1}): 1715 (w, −CO−N−CO), 1528 (m, C−NO$_2$), 1349 (m, C−NO$_2$).

Ru(4-[N-(m-phenyl)-4-amino-1,8-naphthalimide]-2,2′-bipyridine)(bipyridine)$_2$(PF$_6$)$_2$ (4). Ru(4-[N-(m-phenyl)-4-nitro-1,8-naphthalimide]-2,2′-bipyridine)(bipyridine)$_2$Cl$_2$ (0.14 g, 0.12 mmol, 1 equiv) was dissolved in HPLC-grade MeOH and 10% Pd/C added. The reaction mixture was subjected to 3 atm of H$_2$ for 24 h before being filtered through a Celite plug and the solvent removed under reduced pressure, giving the product as an orange solid (0.13 g, 98%). Calcd for C$_{48}$H$_{34}$F$_{12}$N$_8$O$_2$P$_2$Ru·2.5CH$_3$CN: C, 50.99; H, 3.35; N, 11.78. Found: C, 51.14; H, 3.65; N, 11.54. Accurate MS. Calcd for C$_{48}$H$_{43}$N$_8$O$_2$Ru (M^{2+}): m/z 856.1848. Found: m/z 856.1818. ^{1}H NMR (CD$_3$CN, 600 MHz): δ_H 8.71 (1H, s, Ar−H), 8.54 (5H, m, 5 × Ar−H), 8.35 (1H, d, J = 7.1 Hz, Ar−H), 8.23 (1H, d, J = 8.3 Hz, Ar−H), 8.09 (5H, m, 5 × Ar−H), 7.97 (1H, t, J = 7.9 Hz, Ar−H), 7.80 (1H, d, J = 4.9 Hz, Ar−H), 7.75 (5H, m, 5 × Ar−H), 7.66 (1H, d, J = 6.0 Hz, Ar−H), 7.63 (1H, d, J = 7.6 Hz, Ar−H), 7.54 (1H, t, J = 7.6 Hz, Ar−H), 7.50−7.38 (5H, m, 7 × Ar−H), 6.70 (1H, br d, J = 6.8 Hz, NH_2). ^{13}C NMR (CH$_3$CN, 150 MHz): δ_C 164.6, 163.9, 157.4, 156.9, 156.8, 156.78, 156.77, 151.8, 151.6, 151.5, 151.4, 151.3, 147.4, 138.2, 137.8, 137.7, 137.6, 135.8, 133.6, 131.3, 131.1, 129.9, 128.6, 128.2, 127.5, 127.49, 127.48, 126.1, 124.5, 124.3, 124.2, 124.1, 123.9, 122.0, 121.1, 119.4, 109.1, 108.5. IR ν_{max} (cm^{-1}): 3354 (w, −NH$_2$), 1684 (m, −CO−N−CO−), 1634 (s, −NH$_2$).

■ ASSOCIATED CONTENT

Ⓢ Supporting Information

The Supporting Information is available free of charge at https://pubs.acs.org/doi/10.1021/acs.inorgchem.0c01395.

> Details of all general experimental techniques (pages 2−5), synthesis details of **7**, **9**, **12**, and **13** and characterization of the spectra of compounds **1−4**, **7**, **9**, **12**, and **13** (pages 6−16), photophysical investigations for each system as well as tables containing binding constants (pages 17−32), and additional biological data (pages 33−38) (PDF)

Accession Codes

CCDC 2002583 contains the supplementary crystallographic data for this paper. These data can be obtained free of charge via www.ccdc.cam.ac.uk/data_request/cif, or by emailing data_request@ccdc.cam.ac.uk, or by contacting The Cambridge Crystallographic Data Centre, 12 Union Road, Cambridge CB2 1EZ, UK; fax: +44 1223 336033.

■ AUTHOR INFORMATION

Corresponding Authors

Robert B. P. Elmes − *Department of Chemistry, Maynooth University, National University of Ireland, Maynooth W23 F2K8, County Kildare, Ireland; Synthesis and Solid State Pharmaceutical Centre (SSPC), Limerick, County Limerick, Ireland;* ⓞ orcid.org/0000-0001-7898-903X; Phone: +353 1708 4615; Email: robert.elmes@mu.ie

Susan J. Quinn − *School of Chemistry, University College Dublin, Dublin 4, Ireland; Synthesis and Solid State Pharmaceutical Centre (SSPC), Limerick, County Limerick, Ireland;* ⓞ orcid.org/0000-0002-7773-8842; Phone: +353 7162407; Email: susan.quinn@ucd.ie

Thorfinnur Gunnlaugsson − *School of Chemistry, Trinity Biomedical Sciences Institute, Trinity College Dublin (TCD), The University of Dublin, Dublin 2, Ireland; Synthesis and Solid State Pharmaceutical Centre (SSPC), Limerick, County Limerick, Ireland;* ⓞ orcid.org/0000-0003-4814-6853; Phone: +353 896 3459; Email: gunnlaut@tcd.ie

Authors

Gary J. Ryan − *School of Chemistry, Trinity Biomedical Sciences Institute, Trinity College Dublin (TCD), The University of Dublin, Dublin 2, Ireland*

Maria Luisa Erby − *School of Biochemistry and Immunology, Trinity Biomedical Sciences Institute, Trinity College Dublin, The University of Dublin, Dublin 2, Ireland*

Daniel O. Frimannsson − *School of Chemistry, Trinity Biomedical Sciences Institute, Trinity College Dublin (TCD), The University of Dublin, Dublin 2, Ireland; School of Medicine, Institute of Molecular Medicine, St. James's Hospital, Trinity College Dublin, Dublin 8, Ireland*

Jonathan A. Kitchen − *School of Chemistry, Trinity Biomedical Sciences Institute, Trinity College Dublin (TCD), The University of Dublin, Dublin 2, Ireland; Chemistry, School of Natural and Computational Sciences, Massey University, Auckland 0745, New Zealand;* ⓞ orcid.org/0000-0002-7139-5666

Mark Lawler − *Institute for Health Sciences, Centre for Cancer Research and Cell Biology, School of Medicine, Dentistry and Biomedical Sciences, Queen's University of Belfast, Belfast BT9 7BL, Northern Ireland*

D. Clive Williams − *School of Biochemistry and Immunology, Trinity Biomedical Sciences Institute, Trinity College Dublin, The University of Dublin, Dublin 2, Ireland*

Complete contact information is available at:
https://pubs.acs.org/10.1021/acs.inorgchem.0c01395

Notes

The authors declare no competing financial interest.

■ REFERENCES

(1) Vougioukalakis, G. C.; Philippopoulos, A. I.; Stergiopoulos, T.; Falaras, P. Contributions to the development of ruthenium-based sensitizers for dye-sensitized solar cells. *Coord. Chem. Rev.* **2011**, *255* (21), 2602−2621.

(2) Yin, J.-F.; Velayudham, M.; Bhattacharya, D.; Lin, H.-C.; Lu, K.-L. Structure optimization of ruthenium photosensitizers for efficient dye-sensitized solar cells − A goal toward a "bright" future. *Coord. Chem. Rev.* **2012**, *256* (23), 3008−3035.

(3) Prier, C. K.; Rankic, D. A.; MacMillan, D. W. C. Visible Light Photoredox Catalysis with Transition Metal Complexes: Applications in Organic Synthesis. *Chem. Rev.* **2013**, *113* (7), 5322−5363.

(4) Tucker, J. W.; Stephenson, C. R. J. Shining Light on Photoredox Catalysis: Theory and Synthetic Applications. *J. Org. Chem.* **2012**, *77* (4), 1617−1622.

(5) Bonnet, S.; Collin, J.-P. Ruthenium-based light-driven molecular machine prototypes: synthesis and properties. *Chem. Soc. Rev.* **2008**, *37* (6), 1207−1217.

(6) Colasson, B.; Credi, A.; Ragazzon, G. Light-driven molecular machines based on ruthenium(II) polypyridine complexes: Strategies and recent advances. *Coord. Chem. Rev.* **2016**, *325*, 125−134.

(7) Poynton, F. E.; Bright, S. A.; Blasco, S.; Williams, D. C.; Kelly, J. M.; Gunnlaugsson, T. The development of ruthenium(ii) polypyridyl complexes and conjugates for in vitro cellular and in vivo applications. *Chem. Soc. Rev.* **2017**, *46* (24), 7706−7756.

(8) Cosgrave, L.; Devocelle, M.; Forster, R. J.; Keyes, T. E. Multimodal cell imaging by ruthenium polypyridyl labelled cell penetrating peptides. *Chem. Commun.* **2010**, *46* (1), 103−105.

(9) Blackmore, L.; Moriarty, R.; Dolan, C.; Adamson, K.; Forster, R. J.; Devocelle, M.; Keyes, T. E. Peptide directed transmembrane transport and nuclear localization of Ru(ii) polypyridyl complexes in mammalian cells. *Chem. Commun.* **2013**, *49* (26), 2658−2660.

(10) Friedman, A. E.; Chambron, J. C.; Sauvage, J. P.; Turro, N. J.; Barton, J. K. A molecular light switch for DNA: Ru(bpy)2(dppz)2+. *J. Am. Chem. Soc.* **1990**, *112* (12), 4960−4962.

(11) Gill, M. R.; Thomas, J. A. Ruthenium(ii) polypyridyl complexes and DNA—from structural probes to cellular imaging and therapeutics. *Chem. Soc. Rev.* **2012**, *41* (8), 3179−3192.

(12) TOSSI, A. B.; KELLY, J. M. A STUDY OF SOME POLYPYRIDYLRUTHENIUM(II) COMPLEXES AS DNA BINDERS AND PHOTOCLEAVAGE REAGENTS. *Photochem. Photobiol.* **1989**, *49* (5), 545−556.

(13) Mesmaeker, A. K.-D.; Orellana, G.; Barton, J. K.; Turro, N. J. LIGAND-DEPENDENT INTERACTION OF RUTHENIUM(II) POLYPYRIDYL COMPLEXES WITH DNA PROBED BY EMISSION SPECTROSCOPY. *Photochem. Photobiol.* **1990**, *52* (3), 461−472.

(14) Elmes, R. B. P.; Kitchen, J. A.; Williams, D. C.; Gunnlaugsson, T. Pushing the limit: synthesis, photophysical and DNA binding studies of a NIR-emitting Ru(ii)-polypyridyl probe with 'light switch' behaviour. *Dalton Transactions* **2012**, *41* (22), 6607−6610.

(15) Boynton, A. N.; Marcélis, L.; McConnell, A. J.; Barton, J. K. A Ruthenium(II) Complex as a Luminescent Probe for DNA Mismatches and Abasic Sites. *Inorg. Chem.* **2017**, *56* (14), 8381−8389.

(16) Hall, J. P.; O'Sullivan, K.; Naseer, A.; Smith, J. A.; Kelly, J. M.; Cardin, C. J. Structure determination of an intercalating ruthenium dipyridophenazine complex which kinks DNA by semiintercalation of a tetraazaphenanthrene ligand. *Proc. Natl. Acad. Sci. U. S. A.* **2011**, *108* (43), 17610−17614.

(17) Niyazi, H.; Hall, J. P.; O'Sullivan, K.; Winter, G.; Sorensen, T.; Kelly, J. M.; Cardin, C. J. Crystal structures of Λ-[Ru(phen)2dppz]2+ with oligonucleotides containing TA/TA and AT/AT steps show two intercalation modes. *Nat. Chem.* **2012**, *4* (8), 621−628.

(18) McQuaid, K.; Abell, H.; Gurung, S. P.; Allan, D. R.; Winter, G.; Sorensen, T.; Cardin, D. J.; Brazier, J. A.; Cardin, C. J.; Hall, J. P. Structural Studies Reveal Enantiospecific Recognition of a DNA G-Quadruplex by a Ruthenium Polypyridyl Complex. *Angew. Chem., Int. Ed.* **2019**, *58* (29), 9881.

(19) Keane, P. M.; Hall, J. P.; Poynton, F. E.; Poulsen, B. C.; Gurung, S. P.; Clark, I. P.; Sazanovich, I. V.; Towrie, M.; Gunnlaugsson, T.; Quinn, S. J.; Cardin, C. J.; Kelly, J. M. Inosine Can Increase DNA's Susceptibility to Photo-oxidation by a RuII

Complex due to Structural Change in the Minor Groove. *Chem. - Eur. J.* **2017**, *23* (43), 10344−10351.

(20) Cardin, C. J.; Kelly, J. M.; Quinn, S. J. Photochemically active DNA-intercalating ruthenium and related complexes − insights by combining crystallography and transient spectroscopy. *Chemical Science* **2017**, *8* (7), 4705−4723.

(21) Boynton, A. N.; Marcélis, L.; Barton, J. K. [Ru(Me4phen)-2dppz]2+, a Light Switch for DNA Mismatches. *J. Am. Chem. Soc.* **2016**, *138* (15), 5020−5023.

(22) Song, H.; Kaiser, J. T.; Barton, J. K. Crystal structure of Δ-[Ru(bpy)2dppz]2+ bound to mismatched DNA reveals side-by-side metalloinsertion and intercalation. *Nat. Chem.* **2012**, *4*, 615.

(23) Hall, J. P.; Poynton, F. E.; Keane, P. M.; Gurung, S. P.; Brazier, J. A.; Cardin, D. J.; Winter, G.; Gunnlaugsson, T.; Sazanovich, I. V.; Towrie, M.; Cardin, C. J.; Kelly, J. M.; Quinn, S. J. Monitoring one-electron photo-oxidation of guanine in DNA crystals using ultrafast infrared spectroscopy. *Nat. Chem.* **2015**, *7*, 961.

(24) Ghesquiere, J.; Le Gac, S.; Marcelis, L.; Moucheron, C.; Kirsch - De Mesmaeker, A. What Does the Future Hold for Photo-Oxidizing RuII Complexes with Polyazaaromatic Ligands in Medicinal Chemistry? *Curr. Top. Med. Chem.* **2012**, *12* (3), 185−196.

(25) Mattiuzzi, A.; Jabin, I.; Moucheron, C.; Kirsch-De Mesmaeker, A. Ru-TAP complexes with btz and pytz ligands: novel candidates as photooxidizing agents. *Dalton Transactions* **2011**, *40* (28), 7395−7402.

(26) Knoll, J. D.; Turro, C. Control and utilization of ruthenium and rhodium metal complex excited states for photoactivated cancer therapy. *Coord. Chem. Rev.* **2015**, *282−283*, 110−126.

(27) Kelly, J. M.; McConnell, D. J.; OhUigin, C.; Tossi, A. B.; Mesmaeker, A. K.-D.; Masschelein, A.; Nasielski, J. Ruthenium polypyridyl complexes; their interaction with DNA and their role as sensitisers for its photocleavage. *J. Chem. Soc., Chem. Commun.* **1987**, *24*, 1821−1823.

(28) Mari, C.; Pierroz, V.; Rubbiani, R.; Patra, M.; Hess, J.; Spingler, B.; Oehninger, L.; Schur, J.; Ott, I.; Salassa, L.; Ferrari, S.; Gasser, G. DNA Intercalating RuII Polypyridyl Complexes as Effective Photosensitizers in Photodynamic Therapy. *Chem. - Eur. J.* **2014**, *20* (44), 14421−14436.

(29) Huang, H.; Yu, B.; Zhang, P.; Huang, J.; Chen, Y.; Gasser, G.; Ji, L.; Chao, H. Highly Charged Ruthenium(II) Polypyridyl Complexes as Lysosome-Localized Photosensitizers for Two-Photon Photodynamic Therapy. *Angew. Chem., Int. Ed.* **2015**, *54* (47), 14049−14052.

(30) Mari, C.; Pierroz, V.; Ferrari, S.; Gasser, G. Combination of Ru(ii) complexes and light: new frontiers in cancer therapy. *Chemical Science* **2015**, *6* (5), 2660−2686.

(31) Clarke, M. J. Ruthenium metallopharmaceuticals. *Coord. Chem. Rev.* **2002**, *232* (1−2), 69−93.

(32) Shum, J.; Leung, P. K.-K.; Lo, K. K.-W. Luminescent Ruthenium(II) Polypyridine Complexes for a Wide Variety of Biomolecular and Cellular Applications. *Inorg. Chem.* **2019**, *58* (4), 2231−2247.

(33) Jarman, P. J.; Noakes, F.; Fairbanks, S.; Smitten, K.; Griffiths, I. K.; Saeed, H. K.; Thomas, J. A.; Smythe, C. Exploring the Cytotoxicity, Uptake, Cellular Response, and Proteomics of Mono- and Dinuclear DNA Light-Switch Complexes. *J. Am. Chem. Soc.* **2019**, *141* (7), 2925−2937.

(34) Li, X.; Gorle, A. K.; Sundaraneedi, M. K.; Keene, F. R.; Collins, J. G. Kinetically-inert polypyridylruthenium(II) complexes as therapeutic agents. *Coord. Chem. Rev.* **2018**, *375*, 134−147.

(35) Thota, S.; Rodrigues, D. A.; Crans, D. C.; Barreiro, E. J. Ru(II) Compounds: Next-Generation Anticancer Metallotherapeutics? *J. Med. Chem.* **2018**, *61* (14), 5805−5821.

(36) Zeng, L.; Gupta, P.; Chen, Y.; Wang, E.; Ji, L.; Chao, H.; Chen, Z.-S. The development of anticancer ruthenium(ii) complexes: from single molecule compounds to nanomaterials. *Chem. Soc. Rev.* **2017**, *46* (19), 5771−5804.

(37) Cloonan, S. M.; Elmes, R. B. P.; Erby, M.; Bright, S. A.; Poynton, F. E.; Nolan, D. E.; Quinn, S. J.; Gunnlaugsson, T.;

Williams, D. C. Detailed Biological Profiling of a Photoactivated and Apoptosis Inducing pdppz Ruthenium(II) Polypyridyl Complex in Cancer Cells. *J. Med. Chem.* **2015**, *58* (11), 4494−4505.

(38) Elias, B.; Creely, C.; Doorley, G. W.; Feeney, M. M.; Moucheron, C.; Kirsch-DeMesmaeker, A.; Dyer, J.; Grills, D. C.; George, M. W.; Matousek, P.; Parker, A. W.; Towrie, M.; Kelly, J. M. Photooxidation of guanine by a ruthenium dipyridophenazine complex intercalated in a double-stranded polynucleotide monitored directly by picosecond visible and infrared transient absorption spectroscopy. *Chem. - Eur. J.* **2008**, *14* (1), 369−375.

(39) Elias, B.; Kirsch-De Mesmaeker, A. Photo-reduction of polyazaaromatic Ru(II) complexes by biomolecules and possible applications. *Coord. Chem. Rev.* **2006**, *250* (13−14), 1627−1641.

(40) Weynand, J.; Diman, A.; Abraham, M.; Marcélis, L.; Jamet, H.; Decottignies, A.; Dejeu, J.; Defrancq, E.; Elias, B. Towards the Development of Photo-Reactive Ruthenium(II) Complexes Targeting Telomeric G-Quadruplex DNA. *Chem. - Eur. J.* **2018**, *24* (72), 19216−19227.

(41) Archer, S. A.; Raza, A.; Dröge, F.; Robertson, C.; Auty, A. J.; Chekulaev, D.; Weinstein, J. A.; Keane, T.; Meijer, A. J. H. M.; Haycock, J. W.; MacNeil, S.; Thomas, J. A. A dinuclear ruthenium(II) phototherapeutic that targets duplex and quadruplex DNA. *Chemical Science* **2019**, *10* (12), 3502−3513.

(42) Reichardt, C.; Monro, S.; Sobotta, F. H.; Colón, K. L.; Sainuddin, T.; Stephenson, M.; Sampson, E.; Roque, J.; Yin, H.; Brendel, J. C.; Cameron, C. G.; McFarland, S.; Dietzek, B. Predictive Strength of Photophysical Measurements for in Vitro Photobiological Activity in a Series of Ru(II) Polypyridyl Complexes Derived from π-Extended Ligands. *Inorg. Chem.* **2019**, *58* (5), 3156−3166.

(43) Keane, P. M.; Kelly, J. M. Transient absorption and time-resolved vibrational studies of photophysical and photochemical processes in DNA-intercalating polypyridyl metal complexes or cationic porphyrins. *Coord. Chem. Rev.* **2018**, *364*, 137−154.

(44) Jakubaszek, M.; Goud, B.; Ferrari, S.; Gasser, G. Mechanisms of action of Ru(II) polypyridyl complexes in living cells upon light irradiation. *Chem. Commun.* **2018**, *54* (93), 13040−13059.

(45) Monro, S.; Colón, K. L.; Yin, H.; Roque, J.; Konda, P.; Gujar, S.; Thummel, R. P.; Lilge, L.; Cameron, C. G.; McFarland, S. A. Transition Metal Complexes and Photodynamic Therapy from a Tumor-Centered Approach: Challenges, Opportunities, and Highlights from the Development of TLD1433. *Chem. Rev.* **2019**, *119* (2), 797−828.

(46) Rilak Simović, A.; Masnikosa, R.; Bratsos, I.; Alessio, E. Chemistry and reactivity of ruthenium(II) complexes: DNA/protein binding mode and anticancer activity are related to the complex structure. *Coord. Chem. Rev.* **2019**, *398*, 113011.

(47) Elmes, R. B. P.; Orange, K. N.; Cloonan, S. M.; Williams, D. C.; Gunnlaugsson, T. Luminescent Ruthenium(II) Polypyridyl Functionalized Gold Nanoparticles; Their DNA Binding Abilities and Application As Cellular Imaging Agents. *J. Am. Chem. Soc.* **2011**, *133* (40), 15862−15865.

(48) Martinez-Calvo, M.; Orange, K. N.; Elmes, R. B. P.; la Cour Poulsen, B.; Williams, D. C.; Gunnlaugsson, T. Ru(II)-polypyridyl surface functionalised gold nanoparticles as DNA targeting supramolecular structures and luminescent cellular imaging agents. *Nanoscale* **2016**, *8* (1), 563−574.

(49) Elmes, R. B. P.; Erby, M.; Bright, S. A.; Williams, D. C.; Gunnlaugsson, T. Photophysical and biological investigation of novel luminescent Ru(II)-polypyridyl-1,8-naphthalimide Tröger's bases as cellular imaging agents. *Chem. Commun.* **2012**, *48* (20), 2588−2590.

(50) Shanmugaraju, S.; la Cour Poulsen, B.; Arisa, T.; Umadevi, D.; Dalton, H. L.; Hawes, C. S.; Estalayo-Adrián, S.; Savyasachi, A. J.; Watson, G. W.; Williams, D. C.; Gunnlaugsson, T. Synthesis, structural characterisation and antiproliferative activity of a new fluorescent 4-amino-1,8-naphthalimide Tröger's base−Ru(II)−curcumin organometallic conjugate. *Chem. Commun.* **2018**, *54* (33), 4120−4123.

(51) Poulsen, B. C.; Estalayo-Adrián, S.; Blasco, S.; Bright, S. A.; Kelly, J. M.; Williams, D. C.; Gunnlaugsson, T. Luminescent ruthenium polypyridyl complexes with extended 'dppz' like ligands as DNA targeting binders and cellular agents. *Dalton Transactions* **2016**, *45* (45), 18208−18220.

(52) Ryan, G. J.; Poynton, F. E.; Elmes, R. B. P.; Erby, M.; Williams, D. C.; Quinn, S. J.; Gunnlaugsson, T. Unexpected DNA binding properties with correlated downstream biological applications in mono vs. bis-1,8-naphthalimide Ru(II)-polypyridyl conjugates. *Dalton Trans.* **2015**, *44* (37), 16332−16344.

(53) Ryan, G. J.; Quinn, S.; Gunnlaugsson, T. Highly Effective DNA Photocleavage by Novel "Rigid" Ru(bpy)3−4-nitro- and −4-amino-1,8-naphthalimide Conjugates. *Inorg. Chem.* **2008**, *47* (2), 401−403.

(54) Murphy, S.; Bright, S. A.; Poynton, F. E.; McCabe, T.; Kitchen, J. A.; Veale, E. B.; Williams, D. C.; Gunnlaugsson, T. Synthesis, photophysical and cytotoxicity evaluations of DNA targeting agents based on 3-amino-1,8-naphthalimide derived Tröger's bases. *Org. Biomol. Chem.* **2014**, *12* (34), 6610−6623.

(55) Banerjee, S.; Kitchen, J. A.; Bright, S. A.; O'Brien, J. E.; Williams, D. C.; Kelly, J. M.; Gunnlaugsson, T. Synthesis, spectroscopic and biological studies of a fluorescent Pt(II) (terpy) based 1,8-naphthalimide conjugate as a DNA targeting agent. *Chem. Commun.* **2013**, *49* (76), 8522−8524.

(56) Banerjee, S.; Veale, E. B.; Phelan, C. M.; Murphy, S. A.; Tocci, G. M.; Gillespie, L. J.; Frimannsson, D. O.; Kelly, J. M.; Gunnlaugsson, T. Recent advances in the development of 1,8-naphthalimide based DNA targeting binders, anticancer and fluorescent cellular imaging agents. *Chem. Soc. Rev.* **2013**, *42* (4), 1601−1618.

(57) Veale, E. B.; Frimannsson, D. O.; Lawler, M.; Gunnlaugsson, T. 4-Amino-1,8-naphthalimide-Based Tröger's Bases As High Affinity DNA Targeting Fluorescent Supramolecular Scaffolds. *Org. Lett.* **2009**, *11* (18), 4040−4043.

(58) Veale, E. B.; Gunnlaugsson, T. Synthesis, Photophysical, and DNA Binding Studies of Fluorescent Tröger's Base Derived 4-Amino-1,8-naphthalimide Supramolecular Clefts. *J. Org. Chem.* **2010**, *75* (16), 5513−5525.

(59) Aletti, A. B.; Gillen, D. M.; Gunnlaugsson, T. Luminescent/colorimetric probes and (chemo-) sensors for detecting anions based on transition and lanthanide ion receptor/binding complexes. *Coord. Chem. Rev.* **2018**, *354*, 98−120.

(60) Duke, R. M.; Veale, E. B.; Pfeffer, F. M.; Kruger, P. E.; Gunnlaugsson, T. Colorimetric and fluorescent anion sensors: an overview of recent developments in the use of 1,8-naphthalimide-based chemosensors. *Chem. Soc. Rev.* **2010**, *39* (10), 3936−3953.

(61) Veale, E. B.; Gunnlaugsson, T. Bidirectional Photoinduced Electron-Transfer Quenching Is Observed in 4-Amino-1,8-naphthalimide-Based Fluorescent Anion Sensors. *J. Org. Chem.* **2008**, *73* (20), 8073−8076.

(62) Keane, P. M.; Tory, J.; Towrie, M.; Sazanovich, I. V.; Cardin, C. J.; Quinn, S. J.; Hartl, F.; Kelly, J. M.; Long, C. Spectroelectrochemical Studies on [Ru(TAP)2(dppz)]2+—Insights into the Mechanism of its Photosensitized Oxidation of Oligonucleotides. *Inorg. Chem.* **2019**, *58* (1), 663−671.

(63) Marcélis, L.; Rebarz, M.; Lemaur, V.; Fron, E.; De Winter, J.; Moucheron, C.; Gerbaux, P.; Beljonne, D.; Sliwa, M.; Kirsch-De Mesmaeker, A. Photoaddition of Two Guanine Bases to Single Ru-TAP Complexes. Computational Studies and Ultrafast Spectroscopies to Elucidate the pH Dependence of Primary Processes. *J. Phys. Chem. B* **2015**, *119* (12), 4488−4500.

(64) Johansson, O.; Borgstrom, M.; Lomoth, R.; Palmblad, M.; Bergquist, J.; Hammarstrom, L.; Sun, L.; Akermark, B. Electron Donor-Acceptor Dyads Based on Ruthenium(II) Bipyridine and Terpyridine Complexes Bound to Naphthalenediimide. *Inorg. Chem.* **2003**, *42* (9), 2908−2918.

(65) Kitchen, J. A.; Martinho, P. N.; Morgan, G. G.; Gunnlaugsson, T. Synthesis, crystal structure and EPR spectroscopic analysis of novel copper complexes formed from N-pyridyl-4-nitro-1,8-naphthalimide ligands. *Dalton Transactions* **2014**, *43* (17), 6468−6479.

(66) Kitchen, J. A.; Zhang, N.; Carter, A. B.; Fitzpatrick, A. J.; Morgan, G. G. Structural and magnetic properties of dinuclear Cu(II)

complexes featuring triazolyl-naphthalimide ligands. *J. Coord. Chem.* **2016**, *69* (11−13), 2024−2037.

(67) Masschelein, A.; Jacquet, L.; Kirschdemesmaeker, A.; Nasielski, J. Ruthenium Complexes with 1,4,5,8-Tetraazaphenanthrene - Unusual Photophysical Behavior of the Tris-Homoleptic Compound. *Inorg. Chem.* **1990**, *29* (4), 855−860.

(68) Ryan, G. Ph.D. Thesis, The University of Dublin, Dublin, Ireland, 2008.

(69) Del Guerzo, A.; Kirsch-De Mesmaeker, A.; Demeunynck, M.; Lhomme, J. Photophysics of bifunctional Ru(II) complexes bearing an aminoquinoline organic unit. *J. Phys. Chem. B* **1997**, *101* (35), 7012−7021.

(70) Fox, K. R. *Drug−DNA Interaction Protocols.* **1997**; *90.* DOI: 10.1385/089603447X

(71) Carter, M. T.; Rodriguez, M.; Bard, A. J. Voltammetric studies of the interaction of metal chelates with DNA. 2. Tris-chelated complexes of cobalt(III) and iron(II) with 1,10-phenanthroline and 2,2′-bipyridine. *J. Am. Chem. Soc.* **1989**, *111* (24), 8901−8911.

(72) Satyanarayana, S.; Dabrowiak, J. C.; Chaires, J. B. Neither.DELTA.- nor.LAMBDA.-tris(phenanthroline)ruthenium(II) binds to DNA by classical intercalation. *Biochemistry* **1992**, *31* (39), 9319−9324.

(73) Blasius, C. M. A.; Moucheron, C.; Kirsch-De Mesmaeker, A. Photoadducts of Metallic Compounds with Nucleic Acids - Role Played by the Photoelectron Transfer Process and by the TAP and HAT Ligands in the Ru(II) Complexes. *Eur. J. Inorg. Chem.* **2004**, *2004* (20), 3971−3979.

(74) O' Reilly, M.; Kelly, J. M. Binding of bimetallic 1,10-phenanthroline ruthenium(II) complexes to DNA. *New J. Chem.* **1998**, *22*, 215−217.

(75) Lecomte, J.-P.; Mesmaeker, A. K.-D.; Kelly, J. M.; Tossi, A. B.; Görner, H. PHOTO-INDUCED ELECTRON TRANSFER FROM NUCLEOTIDES TO RUTHENIUM-TRIS-1,4,5,8TETRAAZAPHE-NANTHRENE: MODEL FOR PHOTOSENSITIZED DNA OXI-DATION. *Photochem. Photobiol.* **1992**, *55* (5), 681−689.

(76) Jacquet, L.; Kelly, J. M.; Mesmaeker, A. K.-D. Photoadduct between tris(1,4,5,8-tetraazaphenanthrene)ruthenium(II) and guanosine monophosphate-a model for a new mode of covalent binding of metal complexes to DNA. *J. Chem. Soc., Chem. Commun.* **1995**, *9*, 913−914.

(77) Moucheron, C.; Kirsch-De Mesmaeker, A.; Choua, S. Photophysics of Ru(phen)2(PHEHAT)2+: A Novel Light Switch for DNA and Photo-oxidant for Mononucleotides. *Inorg. Chem.* **1997**, *36* (4), 584−592.

(78) Garbett, N. C.; Ragazzon, P. A.; Chaires, J. B. Circular dichroism to determine binding mode and affinity of ligand-DNA interactions. *Nat. Protoc.* **2007**, *2* (12), 3166−3172.

(79) Nordén, B.; Tjerneld, F. Structure of methylene blue−DNA complexes studied by linear and circular dichroism spectroscopy. *Biopolymers* **1982**, *21* (9), 1713−1734.

(80) Stevenson, K. A.; Yen, S. F.; Yang, N. C.; Boykin, D. W.; Wilson, W. D. A substituent constant analysis of the interaction of substituted naphthalene monoimides with DNA. *J. Med. Chem.* **1984**, *27* (12), 1677−1682.

(81) Liu, J.; Zhang, C.; Rees, T. W.; Ke, L.; Ji, L.; Chao, H. Harnessing ruthenium(II) as photodynamic agents: Encouraging advances in cancer therapy. *Coord. Chem. Rev.* **2018**, *363*, 17−28.

(82) Use of Ruthenium Complexes as Photosensitizers in Photo-dynamic Therapy. *Ruthenium Complexes: Photochemical and Bio-medical Applications*; Wiley, 2017; pp 117−137.

(83) Le Gac, S.; Foucart, M.; Gerbaux, P.; Defrancq, E.; Moucheron, C.; Kirsch - De Mesmaeker, A. Photo-reactive RuII-oligonucleotide conjugates: influence of an intercalating ligand on the inter- and intra-strand photo-ligation processes. *Dalton Transactions* **2010**, *39* (40), 9672−9683.